Ginzburg-Landau theory for impure superconductors of polar symmetry

Victor M. Edelstein

Institute of Solid State Physics RAS, 142432 Chernogolovka, Moscow District, Russia

A diagrammatic derivation of the Ginzburg-Landau equations for impure bulk superconductors, whose symmetry group includes the polar axis **c**, is presented. The results obtained are valid at an arbitrary relationship between the critical temperature $k_B T_C$, the inverse impurity scattering time $\hbar/\tau$, and the spin-orbit energy $(\alpha/\hbar) p_F$, where α is the value of the spin-orbit coupling of current carriers, which is inherent in such compounds. The magnetoelectric effect (the spin polarization induced by the supercurrent) is also evaluated under the same conditions. Analogous results for two-dimensional asymmetric superconductors are presented too.

I. INTRODUCTION

Superconductors with broken central symmetry have recently attracted much interest [1,2]. Because of the absence of severe constraints on physical processes imposed on conventional superconductors by the invariance with respect to space parity, such compounds may possess unusual physical properties. One of first examples was the magnetoelectric effect (MEE) [3]—the emergence of the spin magnetization $\mathbf{M} \sim \mathbf{c} \times \mathbf{J}_s$ of the current carriers due to the current $\mathbf{J}_s$ in a superconductor whose symmetry group possesses the polar axis **c**. Recently, quite a number of other extraordinary physical effects of the magnetoelectric nature have been predicted and partly observed (see as reviews Refs. [4,5]).

It is known that the behavior of conventional superconductors in the neighborhood of the critical temperature under equilibrium conditions is satisfactorily described within the framework of the Ginzburg-Landau (GL) theory [6]. One can expect that the same holds true for polar superconductors. A connection between the phenomenological GL approach and the microscopic BCS theory established for the case of clean conventional superconductors [7] was extended to the case of clean polar superconductors as well [8]. It has been revealed an additional parity-odd term in the GL free-energy functional. However, compounds with destroyed mirror symmetry are inevitably many-component ones and already for this reason the amount of lattice imperfections can be large. In addition, some of them are prepared by the arc-melting method or by the method of solid-state reaction. Effects of impurity scattering were also considered for the case of conventional s-wave superconductors [9]. Although the GL theory is intended to describe equilibrium states [6], it turned out that some terms of the GL functional are sensitive to a pure kinetic characteristics—the time of the electron momentum relaxation τ. Later, that theory was extended to the case of singlet d-wave superconductors [10].

The present paper is aimed to derive the GL functional for the case of impure three-dimensional (3D) superconductors of polar symmetry by means of the Feynman diagram technique.

It will be shown that the elastic impurity scattering under the broken space parity condition makes the functional additionally dependent on another kinetic characteristic—the time of the electron spin relaxation τ_S. The mechanism [11–13] behind this relaxation consists of the following. The polar symmetry enters physics of a conductor through the spin-orbit (SO) term in the one-particle Hamiltonian [14–16],

$$H_{\text{SO}} = \alpha\, (\mathbf{p} \times \mathbf{c}) \cdot \boldsymbol{\sigma}, \tag{1}$$

where **p** is the electron momentum, $\boldsymbol{\sigma}$ is the Pauli spin matrix-vector, the unit vector **c** shows the polar axes, and α is the SO constant. (Here and hereafter, we use units in which $\hbar$ and Boltzmann's constant k_B are unity.) The SO energy Eq. (1) can be considered the Zeeman energy in a fictitious magnetic field $\mathbf{B}_f(\mathbf{p}) = \alpha(\mathbf{p} \times \mathbf{c})/\mu_B$. This field stochastically changes its direction by impurity scattering, effectively giving rise to the spin relaxation. If the impurity broadening $1/\tau$ is much larger than the SO energy αp_F at the Fermi momentum p_F, the mechanism described results in the spin relaxation time $\tau_S^{-1} \cong \tau^{-1} \eta^2$, where $\eta = 2\alpha p_F \tau$. Note that the SO constant α enters the problem also through the parameter $\delta = \alpha\, m/p_F$, which is assumed to be very small so all powers of δ in equations in excess of the first will be ignored. The parameter η is allowed below to take any value.

The diagrammatic approach employed markedly differs from the usual one [9] in some points. First, we treat the electromagnetic interaction by means of the perturbation theory rather then through an eikonal (phase-integral) approximation because it proves to be inconvenient to deal with the SO coupling in coordinate space. This approach, though it requires evaluating quite a few Feynman's diagrams, allows one to take account of the SO coupling in a fully controllable way. Another difference is that due to the SO coupling all the constituents of the diagram technique (propagators, vertices, and, what is more important, the so-called impurity ladders) acquire a specific spin structure like that in quantum electrodynamics [17]. Just as in quantum electrodynamics, a technical tool which makes it possible to go from spin-matrix equations into ordinary scalar equations without any

approximations is Fierz identities [18] in a form suited for the particular form of the SO coupling [13,19]. An aspect of impurity scattering should also be noted. The fact is that the SO coupling by lifting the spin degeneracy of the conduction electrons forms two energy branches with positive and negative helicities (the projection of the spin of an electron with momentum **p** on the direction **c** × **p**) with energies which, on the assumption of the isotropic electron mass, are $\epsilon_{\pm}(p, \theta) = \frac{p^2}{2m} \pm \alpha p \sin\theta$, where θ is the angle of the momentum **p** with the polar axis **c**. The gap separating the two branches $\Delta_{SO} = 2\alpha p \sin\theta$ is not a constant function on the old Fermi surface (i.e., at $p = p_F \equiv \sqrt{2m\epsilon_F}$); it turns zero in the points $\theta = 0, \pi$ and reaches a maximum value $\epsilon_{SO} = 2\alpha p_F$ on the circle $\theta = \pi/2$. The scattering of an electron on a single impurity may result in a transition between the branches. Although the one-particle Green's function averaged over impurity positions is diagonal in the helicity index, explicit calculations show that all possible scattering channels contribute comparably into the impurity ladder. Our approach takes account of inter- and intrabranch electron transitions on equal footing.

In impure superconductors, the form of the GL functional found is the same as it is in clean superconductors—in addition to the conventional terms,

$$F_c = \int_{\mathbf{r}} [A|\Delta|^2 + B|\Delta|^4 + C|\mathbf{\Pi}\Delta|^2], \quad (2)$$

the functional also has an anomalous parity-odd term,

$$F_{an} = \frac{D}{2} \int_{\mathbf{r}} (\mathbf{B} \times \mathbf{c}) \cdot (\Delta^* \mathbf{\Pi}\Delta + \Delta \mathbf{\Pi}^* \Delta^*), \quad (3)$$

where $\int_{\mathbf{r}} = \int d^3 r$ and $\mathbf{\Pi} = -i\mathbf{\nabla} + 2\frac{e}{c}\mathbf{A}$. The difference is in a dependence of the coefficients A, B, C, and D on τ in addition to T_C and ϵ_{SO}. Below, all these coefficients will be obtained in an analytical form, which is valid at any values of $T_C\tau$ and $\epsilon_{SO}\tau$. The conventional part of the GL functional weakly depends on the SO coupling, provided that $\delta \ll 1$, whereas the coefficient D at the anomalous term, being proportional to δ, is also controlled by $T_C\tau$ and $T_C\tau_S$. The MEE in 3D dirty superconductors, which has the same physical origin as the anomalous term in the GL functional and can be treated by the same means, is considered as well.

Notice that effects of impurity scattering on the GL functional were recently touched upon [20] as a part of the problem about the upper critical magnetic field in bulk impure noncentrosymmetric superconductors. Above all, that and the present paper differ by models considered. That paper is about a crystal of a cubic symmetry where the SO coupling has the form $\tilde{H}_{SO}(\mathbf{p}) = \gamma_0 \mathbf{p} \cdot \boldsymbol{\sigma}$. Accordingly, the SO splitting of the electron band, $\tilde{\Delta}_{SO}(\mathbf{p}) = 2\gamma_0 p$, is isotropic. Thus, the necessity to deal with the anisotropic SO splitting, $\Delta_{SO} = 2\alpha p \sin\theta$, which is the main difficulty overcome in the present paper, is absent in Ref. [20]. In this respect, the model considered in Ref. [20] is similar to two-dimensional (2D) models. In addition, main calculations of that paper were performed under the assumption that the contributions of the impurity scattering with change of the sign of the helicity may be disregarded if the value of the SO coupling $2\gamma_0 p_F$ substantially exceeds both the elastic scattering rate $1/\tau$ and a cutoff energy (in the BCS self-consistency equation) given by the Debye energy ω_D. As opposed to that, in the present paper it is supposed a
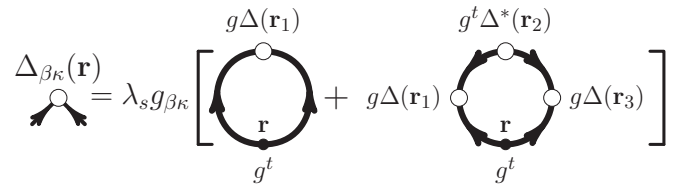

FIG. 1. The diagrammatic equation for $\Delta_{\beta\kappa}(\mathbf{r})$. Here a thick clockwise fermion line denotes $G^{(11)}(i\epsilon_n|\mathbf{r}_1, \mathbf{r}_2)$, while an anticlockwise line denotes $G^{(22)}(i\epsilon_n|\mathbf{r}_1, \mathbf{r}_2)$ defined by Eqs. (4) and (5).

relatively weak SO coupling $2\alpha p_F < \omega_D$ and it is explicitly demonstrated that the interbranch scattering can be taken into account at any relationship between $2\alpha p_F$, $1/\tau$, and T_C.

The case of a 2D asymmetric impure superconductor, which is more amenable to theoretical treatment, is considered too (Appendix I) by the same method that has been applied in the main part of this paper to the case of a bulk superconductor. Recently, this case was discussed by means of the quasiclassical method [21] in the limit of a strong SO coupling $\epsilon_{SO}\tau \gg 1$. We agree with that result.

The paper is organized as follows. In Sec. II, basic equations of the BCS theory and the traditional way [9] to derive the GL expansion is briefly outlined by paying attention to the spin structure of all constituents of the theory. In Sec. III, which is the main part of the paper, the anomalous term in the GL functional is evaluated. Conventional terms are treated more briefly in Sec. IV. The electric current is considered in Sec. V. In Sec. VI, the approach developed in previous sections is applied to the MEE. Section VIII concludes the paper. Details of all calculations are placed in the Appendices. Results for the 2D superconductors are presented in Appendix I.

II. MODEL AND BASIC RELATIONS

We start from the usual expansion [7,9,22,23] of the BCS self-consistency equation in powers of the order parameter, which on the assumption of the s-wave pairing has the form $\Delta_{\gamma\rho}(\mathbf{r}) = g_{\gamma\rho}\Delta(\mathbf{r})$, $g = i\sigma_y$. By cutting off the series on the third term, one gets an equation presented in Fig. 1. The thick fermion lines in the diagrams are components of the Green's matrix function,

$$\widehat{G}_{\alpha\beta}(i\epsilon_n|\mathbf{r}_1, \mathbf{r}_2) = \begin{pmatrix} G^{(11)}(i\epsilon_n|\mathbf{r}_1, \mathbf{r}_2) & 0 \\ 0 & G^{(22)}(i\epsilon_n|\mathbf{r}_1, \mathbf{r}_2) \end{pmatrix}_{\alpha\beta}, \quad (4)$$

which refers to the system in the normal state subject to both the applied magnetic field and the stochastic impurity potential. It obeys the Dyson equation:

$$\widehat{G}(i\epsilon_n|\mathbf{r}_1, \mathbf{r}_2) = \widehat{G}^{(0)}(i\epsilon_n|\mathbf{r}_1 - \mathbf{r}_2) + \int_{\mathbf{r}} \widehat{G}^{(0)}(i\epsilon_n|\mathbf{r}_1 - \mathbf{r})$$
$$\times [\widehat{M}^{(imp)}(\mathbf{r}) + \widehat{M}^{(ef)}(\mathbf{r})]\widehat{G}(i\epsilon_n|\mathbf{r}, \mathbf{r}_2). \quad (5)$$

Here $\widehat{G}^{(0)}(i\epsilon_n|\mathbf{r}_1 - \mathbf{r}_2)$ is the Green's matrix function of the clean system without the external field, which can be found
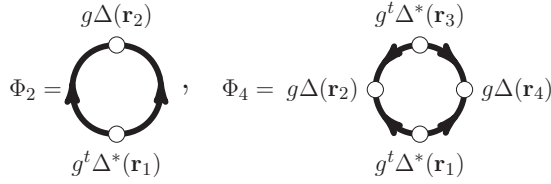
FIG. 2. Loop diagrams for the GL functional.

from the equation of motion

$$\begin{pmatrix} i\epsilon_n - H_{(0)}(-i\boldsymbol{\nabla}_1) & 0 \\ 0 & i\epsilon_n - H_{(0)}^t(i\boldsymbol{\nabla}_1) \end{pmatrix}_{\beta\kappa}$$

$$\times \widehat{G}_{\kappa\rho}^{(0)}(i\epsilon_n|\mathbf{r}_1 - \mathbf{r}_2) = \begin{pmatrix} 1 & 0 \\ 0 & 1 \end{pmatrix} \delta(\mathbf{r}_1 - \mathbf{r}_2)\delta_{\beta\rho}, \quad (6)$$

with the Hamiltonian

$$H_{\gamma\beta}^{(0)}(-i\boldsymbol{\nabla}) = -\frac{\nabla^2}{2m}\delta_{\beta\gamma} + \alpha(-i\boldsymbol{\nabla} \times \mathbf{c}) \cdot \boldsymbol{\sigma}_{\beta\gamma}. \quad (7)$$

Here $\epsilon_n = \pi T(2n+1)$ are fermion frequencies and the superscript t denotes transposition. Also, in Eq. (5),

$$\widehat{M}_{\alpha\beta}^{(\mathrm{imp})}(\mathbf{r}) = \begin{pmatrix} U_{\alpha\beta}^{(\mathrm{imp})}(\mathbf{r}) & 0 \\ 0 & -U_{\alpha\beta}^{t(\mathrm{imp})}(\mathbf{r}) \end{pmatrix} \quad (8)$$

stands for the interaction with the impurity potential and

$$\widehat{M}_{\alpha\beta}^{(\mathrm{ef})}(\mathbf{r}) = \begin{pmatrix} V_{\alpha\beta}^{(\mathrm{ef})}(-i\boldsymbol{\nabla};\mathbf{r}) & 0 \\ 0 & -V_{\alpha\beta}^{t(\mathrm{ef})}(i\boldsymbol{\nabla};\mathbf{r}) \end{pmatrix} \quad (9)$$

accounts for the interaction with the applied magnetic field. Here

$$V_{\gamma\rho}^{(\mathrm{ef})}(-i\boldsymbol{\nabla};\mathbf{r}) = V_{\gamma\rho}^{(\mathrm{par})}(\mathbf{r}) + V_{\gamma\rho}^{(\mathrm{dia})}(-i\boldsymbol{\nabla};\mathbf{r}),$$

$$V_{\gamma\rho}^{(\mathrm{par})}(\mathbf{r}) = \mu_B\boldsymbol{\sigma}_{\gamma\rho} \cdot \mathbf{B}(\mathbf{r}), \quad (10)$$

$$V_{\gamma\rho}^{(\mathrm{dia})}(-i\boldsymbol{\nabla};\mathbf{r}) = \frac{e}{c}\mathbf{v}_{\gamma\rho}(\mathbf{r}) \cdot \mathbf{A}(\mathbf{r}),$$

where

$$\mathbf{v}_{\gamma\rho}(\mathbf{r}) = -i\frac{\boldsymbol{\nabla}}{m}\delta_{\gamma\rho} + \alpha(\mathbf{c} \times \boldsymbol{\sigma})_{\gamma\rho} \quad (11)$$

is the velocity operator and $-e$ is the electron charge. The equation of Fig. 1 is nothing but the stationary condition

$$\frac{\delta F}{\delta\Delta^*(\mathbf{r})} = 0 \quad (12)$$

for the functional

$$F = \frac{1}{\lambda_s}\int_{\mathbf{r}}|\Delta(\mathbf{r})|^2 + \Phi_2 + \frac{1}{2}\Phi_4, \quad (13)$$

where Φ_2 and Φ_4 are quadratic and quartic in $\Delta(\mathbf{r})$, respectively. The corresponding diagrams are depicted in Fig. 2. The next step is an expansion of Φ_2 in powers of the H_{ef}. As a result, the functional Φ_2 transforms into a sum of the conventional term $\Phi_{2.c}$ presented by diagrams in Fig. 3 and the anomalous term $\Phi_{2.\mathrm{an}}$ presented by diagrams in Fig. 4. Unlike Fig. 2, thin solid lines in Figs. 3 and 4 correspond to the normal system subject to the field of nonaveraged impurity potential but without the electron-field interaction. Just as in
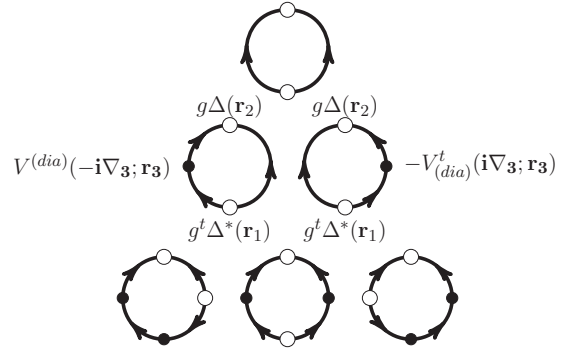
the case of conventional superconductors, an effect of the applied field on Φ_4 can be disregarded.

We assume the potential of randomly distributed impurities of concentration n_{imp} to be short ranged: $U_{\beta\gamma}^{(\mathrm{imp})}(\mathbf{r}) = \sum_i U\delta(\mathbf{r} - \mathbf{R}_i)\delta_{\beta\gamma}$ (then the elastic scattering time τ is given by $\tau^{-1} = 2\pi N(0)n_{\mathrm{imp}}|U|^2$, where $N(0) = mp_F/2\pi^2$ is the density of states on the Fermi level). As is known [24], the averaging over the impurity positions restoring the translational invariance leads to the appearance in diagrams of impurity lines. An impurity line (which is depicted by a dashed line with a cross), contributes $n_{\mathrm{imp}}|U|^2$ if it joins two clockwise or two anticlockwise fermion lines, whereas its contribution is $-n_{\mathrm{imp}}|U|^2$ when it joins a clockwise fermion line to an anticlockwise fermion line. In the case of a conventional superconductor, the sum of impurity insertions (without intersections) into a particular solid line is known [24] to lead to the impurity renormalization of the frequency of the corresponding Green's function,

$$i\epsilon_n \to i\tilde{\epsilon}_n = i\epsilon_n s(\epsilon_n),$$

$$s(\epsilon_n) = 1 + (2\tau|\epsilon_n|)^{-1}. \quad (14)$$

FIG. 3. Diagrammatic representation for $\Phi_{2.c}$. Here the black circle denotes $V^{(\mathrm{dia})}(-i\boldsymbol{\nabla};\mathbf{r})$, when it is placed on a clock-wise solid line, but it denotes $-V^{t(\mathrm{dia})}(i\boldsymbol{\nabla};\mathbf{r})$ being placed on an anticlockwise line.
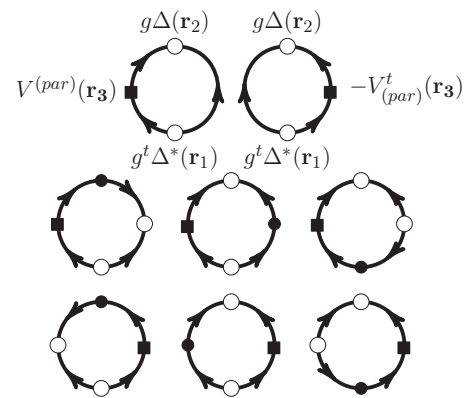

FIG. 4. Diagrammatic representation for $\Phi_{2.\mathrm{an}}$. The black square denotes $V^{(\mathrm{par})}(\mathbf{r})$ if it is placed on a clockwise solid line, whereas being placed on an anticlockwise line it denotes $-V^{t(\mathrm{par})}(\mathbf{r})$. Black circles mean the same as in Fig. 3.

If one neglects corrections quadratic in δ, this result, i.e., the independence of the decay time of an electron state on its helicity, remains valid for our model.

The relation between the momentum and coordinate representations in the presence of the SO coupling has the form

$$\widehat{G}_{\kappa\rho}^{(0)}(i\tilde{\epsilon}_n, \mathbf{r} - \mathbf{r}') = \int_{\mathbf{p}} e^{i\mathbf{p}\cdot(\mathbf{r}-\mathbf{r}')} \begin{pmatrix} G(i\tilde{\epsilon}_n, \mathbf{p}) & 0 \\ 0 & -G^t(-i\tilde{\epsilon}_n, -\mathbf{p}) \end{pmatrix}_{\kappa\rho},$$

$$G_{\kappa\rho}(i\tilde{\epsilon}_n, \mathbf{p}) = \sum_{\nu=\pm} \Pi_{\kappa\rho}^{(\nu)}(\mathbf{p}) G_{(\nu)}(i\tilde{\epsilon}_n, p, \theta), \tag{15}$$

$$\Pi^{(\pm)}(\mathbf{p}) = \frac{1}{2}\left(\sigma_0 \pm \frac{(\mathbf{p} \times \mathbf{c}) \cdot \boldsymbol{\sigma}}{|\mathbf{p} \times \mathbf{c}|}\right).$$

Here $\int_{\mathbf{p}} = \int \frac{d^3 p}{(2\pi)^3}$, $\Pi^{(\pm)}(\mathbf{p})$ is the operator of projection onto states with a definite helicity,

$$G_{(\nu)}(i\tilde{\epsilon}_n, p, \theta) = [i\tilde{\epsilon}_n - \xi_{(\nu)}(p, \theta)]^{-1}, \tag{16}$$

and $\xi_{(\pm)}(p, \theta) = \epsilon_\pm(p, \theta) - \mu$. For the following, it is convenient to also introduce the reversed Green's function, $G_{\kappa\rho}^{(\text{rev})}(i\epsilon_n, \mathbf{p})$ via the equation

$$-G_{\kappa\rho}^t(-i\tilde{\epsilon}_n, -\mathbf{p}) = g_{\kappa\gamma}^t G_{\gamma\beta}^{(\text{rev})}(i\tilde{\epsilon}_n, \mathbf{p}) g_{\beta\rho}. \tag{17}$$

Then

$$G_{\kappa\rho}^{(\text{rev})}(i\tilde{\epsilon}_n, \mathbf{p}) = \sum_{\nu=\pm} \Pi_{\kappa\rho}^{(\nu)}(\mathbf{p}) G_{(\nu)}^{(\text{rev})}(i\tilde{\epsilon}_n, p, \theta),$$

$$G_{(\nu)}^{(\text{rev})}(i\tilde{\epsilon}_n, p, \theta) = [i\tilde{\epsilon}_n + \xi_{(\nu)}(p, \theta)]^{-1}. \tag{18}$$

In deriving Eqs. (18), use has been made of the equality

$$g\Pi^{t(\pm)}(-\mathbf{p})g^t = \Pi^{(\pm)}(\mathbf{p}), \tag{19}$$

which is a consequence of the easy verified identity $g\sigma^t g^t = -\boldsymbol{\sigma}$. Equations (10) in momentum space take the form

$$V_{\beta\gamma}^{(\text{par})}(\mathbf{r}) \rightarrow V_{\beta\gamma}^{(\text{par})}(\mathbf{q}) = \mu_B \boldsymbol{\sigma}_{\beta\gamma} \cdot \mathbf{B}(\mathbf{q}),$$

$$V_{\beta\gamma}^{(\text{dia})}(-i\boldsymbol{\nabla}; \mathbf{r}) \rightarrow V_{\beta\gamma}^{(\text{dia})}(\mathbf{p}; \mathbf{q}) = \frac{e}{c}\mathbf{v}_{\beta\gamma}(\mathbf{p}) \cdot \mathbf{A}(\mathbf{q}). \tag{20}$$

with

$$\mathbf{v}_{\beta\gamma}(\mathbf{p}) = \frac{\mathbf{p}}{m}\delta_{\beta\gamma} + \alpha(\mathbf{c} \times \boldsymbol{\sigma})_{\beta\gamma}. \tag{21}$$

Also in the momentum representation, clockwise-directed fermion lines of a diagram become $G_{\beta\gamma}(i\tilde{\epsilon}_n, \mathbf{p})$ while anticlockwise-directed lines become $-G_{\rho\zeta}^t(-i\tilde{\epsilon}_n, -\mathbf{p})$.

III. ANOMALOUS PART OF THE GL FUNCTIONAL

A. Contribution of gap gradient

Without regard to the diamagnetism, only diagrams on the upper line in Fig. 4 are in action. Their form in the momentum representation is shown in Fig. 5. Because $\Delta(\mathbf{r})$, $\mathbf{A}(\mathbf{r})$, and $\mathbf{B}(\mathbf{r})$ are slowly varying compared to the inverse of the Fermi momentum, the Green's functions can be expanded into a series on small parameters q/p_F and q'/p_F as

$$G^{(0)}(i\epsilon_n, \mathbf{p} + \mathbf{q})$$
$$= G^{(0)}(i\epsilon_n, \mathbf{p}) + G^{(0)}(i\epsilon_n, \mathbf{p})[\mathbf{q} \cdot \mathbf{v}(\mathbf{p})]G^{(0)}(i\epsilon_n, \mathbf{p}) + \cdots, \tag{22}$$
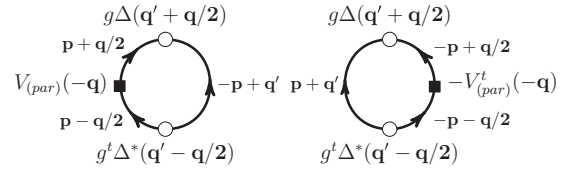

FIG. 5. Diagrams of the upper line in Fig. 4 in the momentum space representation.

or in the diagram language as shown in Fig. 6. Terms of the expansion linear in $\mathbf{q}$ can be shown to cancel themselves while terms linear in $\mathbf{q}'$ transform the diagrams in Fig. 5, first, into the diagrams in Fig. 7 and, further, on account of the impurity scattering, into the diagrams in Fig. 8. The latter diagrams, in addition to elements already defined, also include the impurity ladders (the thick dashed lines defined diagrammatically in Fig. 9) and the impurity dressed gap functions (the gray circles defined by the equation in Fig. 10). The diagrams of Fig. 8 add up to (Appendix C)

$$\Phi_{2.\text{an}} = D\int_{\mathbf{r}} \mathbf{B}(\mathbf{r}) \cdot [\mathbf{c} \times \mathbf{V}(\mathbf{r})], \tag{23}$$

where

$$\mathbf{V}(\mathbf{r}) = \Delta^*(\mathbf{r})\frac{\boldsymbol{\nabla}}{2i}\Delta(\mathbf{r}) - \left(\frac{\boldsymbol{\nabla}}{2i}\Delta^*(\mathbf{r})\right)\Delta(\mathbf{r}). \tag{24}$$

and the coefficient D in its general form is given by Eq. (C21). In the dirty limit ($T_C\tau \ll 1$ and $\epsilon_{\text{SO}}\tau \ll 1$), when the main contribution stems from the diagrams with the impurity ladder, from Eqs. (C21)–(23), it follows:

$$D \simeq 32\alpha\eta^2\left(\frac{mp_F}{3\pi}\right)\mu_B\frac{T_C\tau}{(2\pi T_c)^2}$$
$$\times \sum_{n\geq 0}\left(\frac{1}{2n+1}\right)^2 \frac{1}{2\pi T_c\tau|2n+1| + \frac{1}{3}\eta^2}. \tag{25}$$

B. Contribution of vector potential

In the presence of the magnetic field, six diagrams of the second and third lines in Fig. 4 come into play. After impurity averaging, they turn into 14 diagrams. Half of them, in which the vertex corresponding to $V_{(\text{par})}$ enters the clockwise fermion line, are depicted in Fig. 11. Another half, in which the Zeeman interaction enters the anticlockwise fermion line in the form of $-V_{(\text{par})}^t$, are shown in Fig. 12. For short, momenta of fermion lines are not shown in those figures. They can be restored by means of the momentum conservation law at each vertex, for example, as shown for some chosen diagrams in Appendix D. The total result of evaluation of the diagrams in Figs. 11 and 12 (Appendix D) has the form

$$D\int_{\mathbf{r}}[\mathbf{B}(\mathbf{r}) \times \mathbf{c}] \cdot \frac{2e}{c}\mathbf{A}(\mathbf{r})|\Delta(\mathbf{r})|^2. \tag{26}$$

FIG. 6. Diagrammatic representation of Eq. (22).
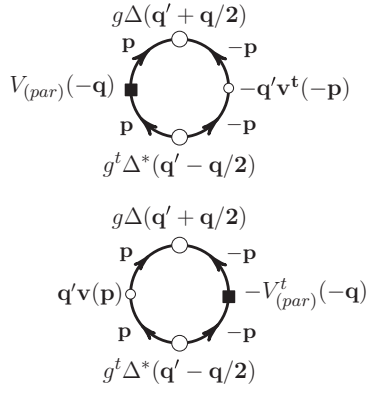
FIG. 7. The result of expansion of the diagrams of Fig. 5 over the small parameter q'/p_F.

Thus, their effect is to replace $\mathbf{V}(\mathbf{r})$ in Eq. (23) with a gauge-invariant combination:

$$\mathbf{V}(\mathbf{r}) + \frac{2e}{c}\mathbf{A}(\mathbf{r})|\Delta(\mathbf{r})|^2$$

$$\equiv \frac{1}{2}[\Delta^*(\mathbf{r})\Pi(\mathbf{r})\Delta(\mathbf{r}) + \Delta(\mathbf{r})\Pi^*(\mathbf{r})\Delta^*(\mathbf{r})]. \quad (27)$$

IV. CONVENTIONAL TERMS

Diagrams responsible for the conventional part of the GL functional fall into four groups. The first three present $\Phi_{2.c}$; their evaluation (Appendix E) shows how the perturbation treatment of the electron-field interaction leads to the gauge-invariant form of the GL functional and also why the conventional part appears to be insensitive to the SO coupling, provided that corrections of the order of δ^2 may be omitted. The forth group is responsible for Φ_4. The first group consists of diagrams which do not include in the diamagnetic interaction with the magnetic field. Initially, there is one such diagram whose skeleton form is shown on the upper line in
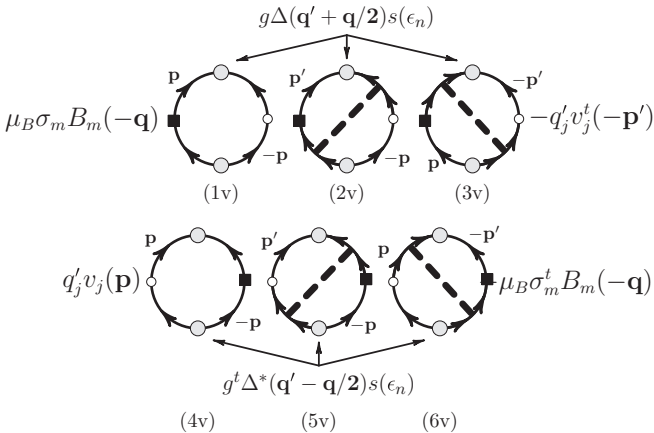

FIG. 8. The diagrams in Fig. 7 with impurity scattering allowed for. The large gray circles denote the impurity-dressed gap function. The thick dashed line in the diagrams (2v), (3v), (5v), and (6v) denotes the impurity ladder.

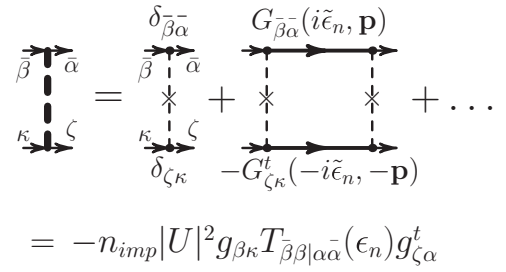$$= -n_{imp}|U|^2 g_{\beta\kappa} T_{\bar{\beta}\beta|\alpha\bar{\alpha}}(\epsilon_n)g_{\zeta\alpha}^t$$

FIG. 9. The impurity ladder. Spin indices on the upper fermion line should be read from left to right, whereas on the lower line they should be read from right to left.

Fig. 13. The **q** expansion converts this diagram into the four ones shown on the second and third lines in Fig. 13. The full form of these diagrams for an impure superconductor is shown in Fig. 26. The sum of the integral term in Eq. (13) and the upper diagram in Fig. 26, just as in the case of a conventional superconductor [9,23], yields the first term in Eq. (2),

$$A\int_{\mathbf{r}}|\Delta(\mathbf{r})|^2, \quad A = \frac{mp_F}{\pi^2}\left(\frac{T-T_C}{T_C}\right), \quad (28)$$

where T_C, upon neglecting corrections proportional to δ^2, depends neither on τ nor on α. Other diagrams in Fig. 26, also just as in the case of an impure conventional superconductor [9], yield

$$C\int_{\mathbf{r}}|\mathbf{\nabla}\Delta(\mathbf{r})|^2,$$

$$C = \frac{p_F^3\tau}{3m\pi^3 T_C}\sum_{n\geqslant 0}\left(\frac{1}{2n+1}\right)^2\frac{1}{1+2\pi T_C\tau(2n+1)]}. \quad (29)$$

The second group consists of diagrams linear in $V_{(dia)}$. They are shown in Fig. 14 in the skeleton form and in Fig. 28 in full form. Their contribution is

$$C\frac{4e}{c}\int_{\mathbf{r}}\mathbf{A}(\mathbf{r})\cdot\mathbf{V}(\mathbf{r}). \quad (30)$$

The skeleton form of diagrams of the third group, which are quadratic in $V_{(dia)}$, are shown in Fig. 15. Their full form is

$$= g_{\beta\kappa}\Delta s(\epsilon_n)$$

FIG. 10. The equation for the impurity-dressed gap function. Spin indices should be read everywhere following a clockwise way beginning from β and ending in κ. The argument of the gap function is dropped here; it depends on the form of a diagram in which the Δ-vertex locates. The method used allows one to deal finally with diagrams in which arguments (momenta) of the fermion lines joined to a given Δ-vertex are opposite to each other and do not depend on the momentum of the gap function corresponding to this vertex; just as it is shown in this figure.
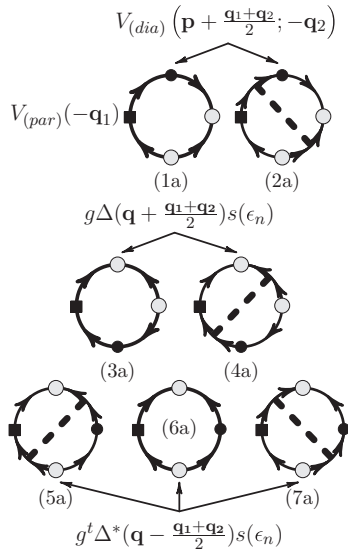
FIG. 11. The result of the impurity averaging of the diagrams of the second line in Fig. 4, which are responsible for a half of F_{an} linear in the vector potential. Their calculation is presented in Appendix D. Arguments of slowly varying (in coordinate space) functions are only pointed out.

shown in Fig. 29. They contribute (Appendix E)

$$C \int_{\mathbf{r}} \left[\frac{2e}{c} \mathbf{A}(\mathbf{r}) \right]^2 |\Delta(\mathbf{r})|^2. \tag{31}$$

Equations (29)–(31) add up to

$$\Phi_{2.c} = C \int_{\mathbf{r}} \left| \left(\frac{\nabla}{i} + \frac{2e}{c} \mathbf{A}(\mathbf{r}) \right) \Delta(\mathbf{r}) \right|^2. \tag{32}$$
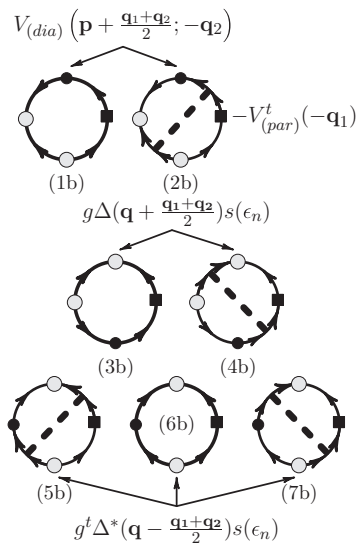

FIG. 12. The diagrams of the third line of Fig. 4 after the averaging over impurity positions. They are responsible for another half of Fan linear in $\mathbf{A}(\mathbf{r})$. Contribution of Figs. 12(1b)–(7b) are equal to that of Figs. 11(1a)–(7a) respectively.
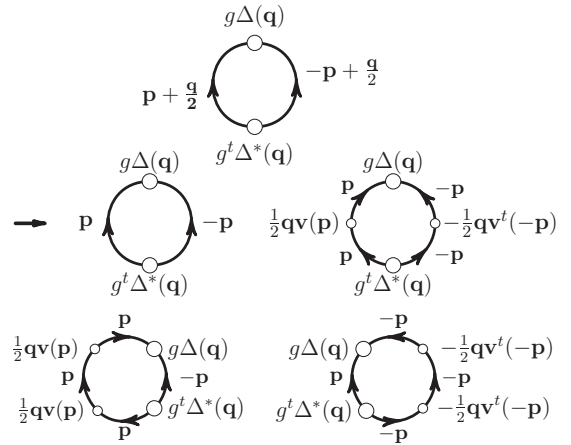

FIG. 13. The contribution to $\Phi_{2.c}$ of zero order in the magnetic field.

Diagrams of the fourth order in $\Delta(\mathbf{r})$, which are shown in Fig. 16 in the skeleton form and in Fig. 31 in the full form, yield (Appendix E)

$$\Phi_4 = 2B \int_{\mathbf{r}} |\Delta(\mathbf{r})|^4, \quad B = \frac{mp_F}{2\pi^4 T_c^2} \sum_{n \geqslant 0} (2n+1)^{-3}, \tag{33}$$

i.e., the same result which holds for a clean superconductor without the SO coupling.

V. ELECTRIC CURRENT

The Fourier transform of the current density is given by

$$\mathbf{J}(\mathbf{q}) = (-e)T \sum_n \int_{\mathbf{p}} \mathrm{Tr} \left\{ \mathbf{v}(\mathbf{p}) G^{(11)} \left(i\epsilon_n | \mathbf{p} + \frac{\mathbf{q}}{2}, \mathbf{p} - \frac{\mathbf{q}}{2} \right) \right\}. \tag{34}$$

An anomalous term in the supercurrent, which is induced by the Zeeman interaction, is depicted in Fig. 17 in skeleton form and in Fig. 18 in the full form due to the impurity scattering. They yield (Appendix F)

$$\mathbf{J}_{an}(\mathbf{r}) = -e\,D[\mathbf{B}(\mathbf{r}) \times \mathbf{c}]|\Delta(\mathbf{r})|^2. \tag{35}$$

A conventional part of the current, which is due to the gradient of the gap function, is shown in Fig. 19 in the skeleton
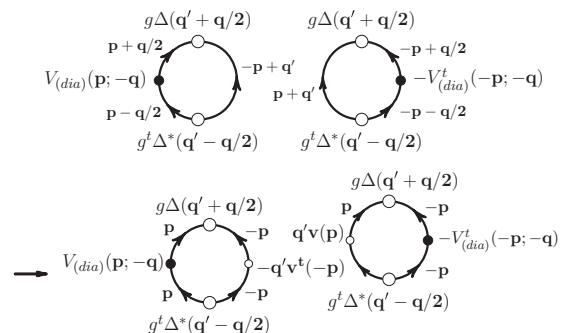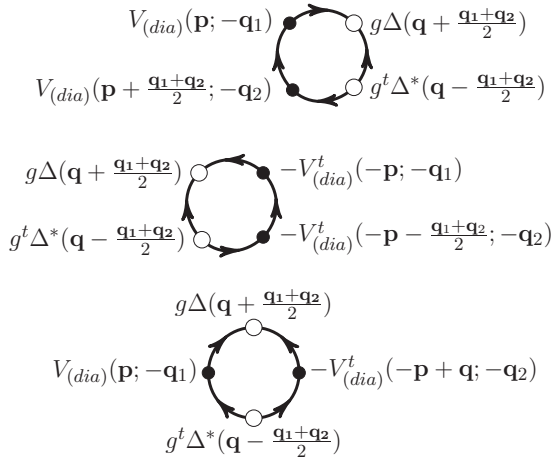

FIG. 14. The diagrams for the term in $\Phi_{2.c}$ linear in the vector potential.

FIG. 15. The contribution to $\Phi_{2.c}$ quadratic in the vector potential.

form and in Fig. 33 (Appendix F) in the full form. The total contribution of diagrams in Fig. 33 is (Appendix F)

$$\mathbf{J}_c^{(1)}(\mathbf{r}) = -2e\,C\mathbf{V}(\mathbf{r}). \tag{36}$$

An effect of diagrams linear in the vector potential $\mathbf{A}(\mathbf{r})$, which are shown in Fig. 20 in the skeleton form and in Fig. 34 (Appendix F) in the full form, is to replace $\mathbf{V}(\mathbf{r})$ in Eq. (36) with a combination $\mathbf{V}(\mathbf{r}) + \frac{2e}{c}\mathbf{A}(\mathbf{r})|\Delta(\mathbf{r})|^2$.

VI. MAGNETOELECTRIC EFFECT

It has been observed [3] that the spin magnetization of a mirror-odd superconductor should be finite if the superconductor is in the current-carrying state. This MEE was first predicted for a 2D superconductor with destroyed up-down symmetry [3]. Later [25], that theory was extended to cover the case of an impure 2D superconductor. Here we consider this effect for a bulk superconductor of polar symmetry within the frame of the model adopted. The Fourier transform of the magnetization density defined by expression

$$\mathbf{M}(\mathbf{q}) = -\mu_B T \sum_{\epsilon_n} \int_{\mathbf{p}} \mathrm{Tr}\left\{\boldsymbol{\sigma} G^{(11)}\left(i\epsilon_n | \mathbf{p} + \frac{\mathbf{q}}{2}, \mathbf{p} - \frac{\mathbf{q}}{2}\right)\right\} \tag{37}$$

can be obtained directly by comparing diagrams for the MEE with analogous diagrams for F_{an}.

At no magnetic field, diagrams for the MEE are shown in Fig. 21. The diagrams in the lower line in Fig. 21 are similar to diagrams in the upper line in Fig. 8; namely, Figs. 21(3u),
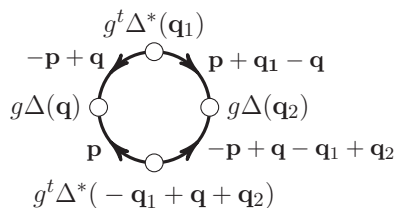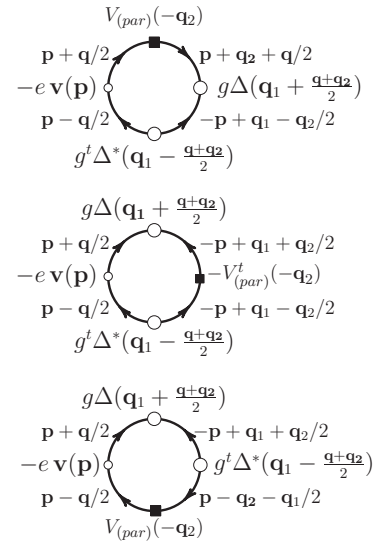

FIG. 16. The skeleton form of the diagram for Φ_4.

FIG. 17. The skeleton diagrams for the anomalous contribution to the current.

(4u), and (5u) correspond to Figs. 8(2v), (1v), and (3v), respectively. Hence

$$\mathbf{M}(\mathbf{r}) = -\tfrac{1}{2}D[\mathbf{c} \times \mathbf{V}(\mathbf{r})]. \tag{38}$$

The applied magnetic field, due to the diamagnetic part of the electron-field interaction, results in the change $\mathbf{V}(\mathbf{r}) \rightarrow \mathbf{V}(\mathbf{r}) + \frac{2e}{c}\mathbf{A}(\mathbf{r})|\Delta(\mathbf{r})|^2$ in Eq. (38). This follows from the comparison of diagrams in Fig. 22 with those in Fig. 11. In addition, due to the paramagnetic part of the interaction, the field also gives rise to a conventional component of the magnetization $M_i^{(c)} = \chi_{ij}B_j$ (Appendix G).
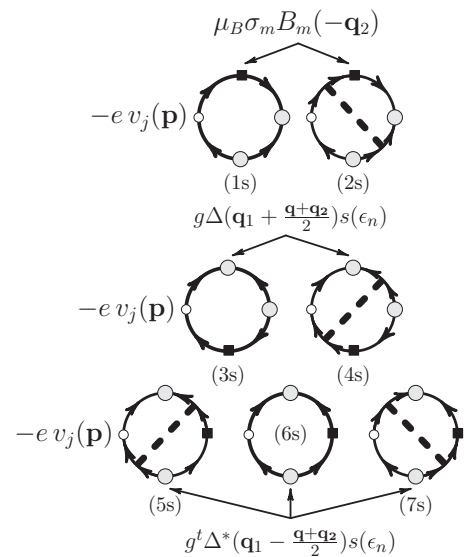

FIG. 18. The contributions to the anomalous part of the current in an impure superconductor. An analysis of the diagrams is presented in Appendix F.
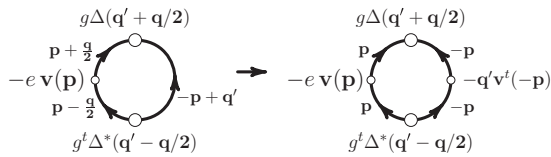
FIG. 19. The conventional contribution to the current due to the gradient of the phase of the gap function in the skeleton form. In the full form, the contribution is presented in Fig. 33.

VII. CONCLUDING REMARKS

In this paper, we have considered two aspects of superconductivity in impure polar symmetry crystals: the GL functional and the MEE near T_C. The results have been obtained in an analytic form and are valid at any relationship between the value of the SO coupling α, the momentum relaxation time τ, and the critical temperature T_C, provided that $\alpha p_F \ll \epsilon_F$. Several conclusions follow from the analysis presented. The first is that the canonical formalism offers a manageable method to derive the GL functional irrespective of the space dimensionality; both the 3D and 2D cases can be treated by the same means. The second is that no physically justified reason is seen for different considerations of the intrabranch and interbranch electron scattering—both the scattering channels are equally important and can be considered on the equal footing. We have also observed that at strong disorder the anomalous terms in the free energy and the spin magnetization are dominated by diagrams containing the impurity ladder.

The physical conclusion is that characteristics of polar superconductors with $\tau_S^{-1} \ll T_C \ll \tau^{-1}$ differ from those with $T_C \ll \tau_S^{-1} \ll \tau^{-1}$. This means that even equilibrium properties of mirror-odd superconductors are subject to the D'yakonov-Perel' mechanism [11,12] of the spin relaxation.
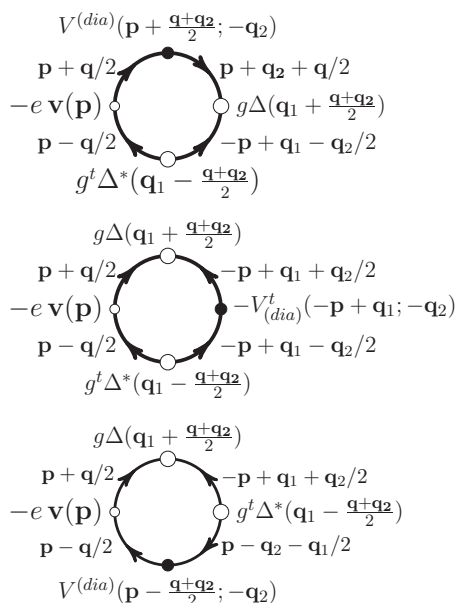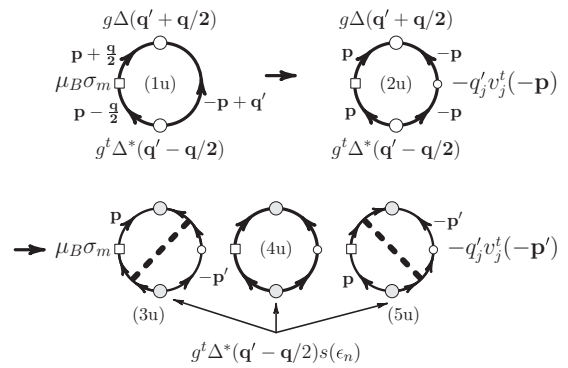

FIG. 21. The skeleton diagram (1u) shows the contribution to the MEE due to space variance of the gap function. The diagram (2u) is a result of the expansion of (1u) into a series of q'/p_F. The diagrams (3u)–(5u) are the final form of the diagram (2u) on account of the impurity scattering.

The distinguished role of the mechanism in various spin-dependent kinetic and optic phenomena in noncentrosymmetric semiconductors is now widely recognized [26]; one may expect the same in noncentrosymmetric superconductors. The approach employed is not confined to equilibrium problems; it can be readily generalized to cover dynamic processes.

Note that the polar symmetry also permits a term in the GL functional of the form $F_{an}^{(2)} \sim \mathbf{B} \cdot (\mathbf{c} \times \mathbf{\nabla}) |\Delta|^2$ (and a corresponding term in the magnetization $M^{(2)} \sim (\mathbf{c} \times \mathbf{\nabla}) |\Delta|^2$). Albeit the expansion of diagrams in Fig. 5 in $\mathbf{q}/p_F$ does give rise to terms of the form, those terms cancel each other within the frame of the microscopic model considered. The symmetry also allows for the average value of the operator of the spin flow $\mathcal{S}_{mi} = \frac{1}{2}(\sigma_m v_i + v_i \sigma_m)$ to be proportional to $c_m [\mathbf{c} \times \mathbf{V}(\mathbf{r})]_i$. However, an analysis (Appendix H) shows that this average value vanishes.

FIG. 20. The conventional contribution to the current due to the vector potential.
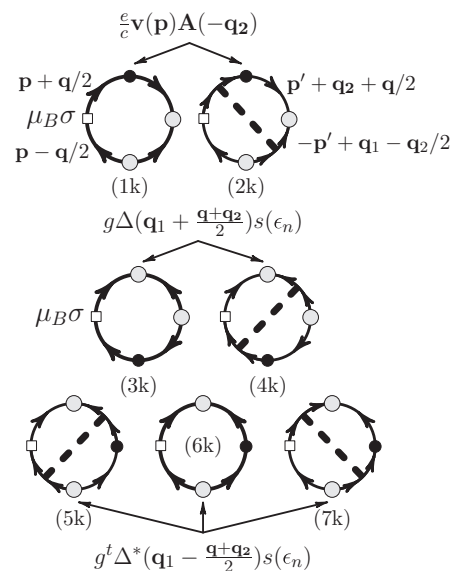

FIG. 22. The diagrams for the contribution to the MEE due to the vector potential $\mathbf{A}(\mathbf{r})$ in the dirty case. Figures 22(1k)–(7k) are analogous to Figs. 11(1a)–(7a)

APPENDIX A: AUXILIARY EQUALITIES

In this Appendix, we list some equalities to be used in the following dealing with diagrams. Let θ be the angle of the momentum $\mathbf{p}$ with the polar axis $\mathbf{c}$. Then

$$\mathbf{p}_\perp \stackrel{\text{def}}{=} \mathbf{p} - \mathbf{c}(\mathbf{c} \cdot \mathbf{p}) = \hat{\mathbf{p}}_\perp p \sin\theta,$$

$$\mathbf{v}(\mathbf{p}) = \mathbf{c}\left(\frac{p}{m}\cos\theta\right) + \hat{\mathbf{p}}_\perp\left(\frac{p}{m}\sin\theta\right) + \alpha(\mathbf{c} \times \boldsymbol{\sigma}). \quad \text{(A1)}$$

The following are some angle integrals:

$$B_m^{(\mu\nu)} \stackrel{\text{def}}{=} \int \frac{d\hat{p}_\perp}{2\pi}\left[\Pi^{(\mu)}(\mathbf{p})\sigma^m\Pi^{(\nu)}(\mathbf{p})\right]_{\kappa\gamma}$$

$$= \frac{1}{4}\begin{pmatrix} \sigma_m - c_m(\mathbf{c}\boldsymbol{\sigma}) & \sigma_m + c_m(\mathbf{c}\boldsymbol{\sigma}) \\ \sigma_m + c_m(\mathbf{c}\boldsymbol{\sigma}) & \sigma_m - c_m(\mathbf{c}\boldsymbol{\sigma}) \end{pmatrix}_{\kappa\gamma}^{(\mu\nu)}, \quad \text{(A2)}$$

$$U_{ij}^{(\mu\nu)} \stackrel{\text{def}}{=} \int \frac{d\hat{p}_\perp}{2\pi}\text{Tr}\left[\sigma_i\Pi^{(\mu)}(\mathbf{p})\sigma_j\Pi^{(\nu)}(\mathbf{p})\right]$$

$$= \frac{1}{2}\begin{pmatrix} \delta_{ij} - c_i c_j & \delta_{ij} + c_i c_j \\ \delta_{ij} + c_i c_j & \delta_{ij} - c_i c_j \end{pmatrix}_{(\mu\nu)}, \quad \text{(A3)}$$

$$V_j^{(\mu\nu)}(\theta) \stackrel{\text{def}}{=} \int \frac{d\hat{p}_\perp}{2\pi}\left[\Pi^{(\mu)}(\mathbf{p})v^j(\mathbf{p})\Pi^{(\nu)}(\mathbf{p})\right]_{\kappa\gamma}$$

$$= \frac{1}{2}c^j\left(\frac{p}{m}\cos\theta\right)\begin{pmatrix} 1 & 0 \\ 0 & 1 \end{pmatrix}_{(\mu\nu)}\delta_{\kappa\gamma} + \frac{1}{4}(\mathbf{c} \times \boldsymbol{\sigma})_{\kappa\gamma}^j$$

$$\times \begin{pmatrix} \frac{p}{m}\sin\theta + \alpha & \alpha \\ \alpha & -\left(\frac{p}{m}\sin\theta - \alpha\right) \end{pmatrix}_{(\mu\nu)}, \quad \text{(A4)}$$

$$S_{mj}^{(\mu\nu)}(\theta) \stackrel{\text{def}}{=} \int \frac{d\hat{p}_\perp}{2\pi}\text{Tr}\left\{\sigma_m\Pi^{(\mu)}(\mathbf{p})v_j(\mathbf{p})\Pi^{(\nu)}(\mathbf{p})\right\}$$

$$= \frac{1}{2}e_{mjs}c^s\begin{pmatrix} \frac{p}{m}\sin\theta + \alpha & \alpha \\ \alpha & -\frac{p}{m}\sin\theta + \alpha \end{pmatrix}_{(\mu\nu)}, \quad \text{(A5)}$$

$$P_{ij}^{(\mu\nu)}(\theta) \stackrel{\text{def}}{=} \int \frac{d\hat{p}_\perp}{2\pi}\text{Tr}\left\{v^i(\mathbf{p})\Pi^{(\mu)}(\mathbf{p})v^j(\mathbf{p})\Pi^{(\nu)}(\mathbf{p})\right\}$$

$$= c_i c_j\left(\frac{p}{m}\cos\theta\right)^2\begin{pmatrix} 1 & 0 \\ 0 & 1 \end{pmatrix}^{(\mu\nu)} + \frac{1}{2}(\delta_{ij} - c_i c_j)$$

$$\times \begin{pmatrix} \left(\frac{p}{m}\sin\theta + \alpha\right)^2 & \alpha^2 \\ \alpha^2 & \left(\frac{p}{m}\sin\theta - \alpha\right)^2 \end{pmatrix}_{(\mu\nu)}. \quad \text{(A6)}$$

Below are radial integrals whose values should be evaluated with the accuracy up to terms linear in $\delta = \alpha/v_F$. Because energy bands of electrons with positive and negative helicities

are different, $\xi_{(\pm)}(p, \theta) = \xi \pm \alpha p \sin\theta$ $(\xi = \frac{p^2}{2m} - \mu)$, there are two Fermi momenta at a given θ, whose values with the adopted accuracy are

$$p_\pm(\theta) \cong p_F[1 \mp \delta(\theta)]. \quad \text{(A7)}$$

Near these momenta, the energy branches behave as

$$\xi_{(\pm)}(p, \theta) \cong \xi[1 \pm \delta(\theta)] \pm \alpha(\theta)p_F, \quad \text{(A8)}$$

where

$$\alpha(\theta) = \alpha \sin\theta, \quad \delta(\theta) = \frac{\alpha(\theta)}{v_F}. \quad \text{(A9)}$$

Also, with the adopted accuracy,

$$\frac{p(\xi)}{p_F} \cong \begin{cases} 1 - \delta(\theta) + \frac{\xi_{(+)}}{v_F p_F}, & |p - p_+(\theta)| \ll p_F \\ 1 + \delta(\theta) + \frac{\xi_{(-)}}{v_F p_F}, & |p - p_-(\theta)| \ll p_F \end{cases} \quad \text{(A10)}$$

and

$$\frac{d\xi}{d\xi_{(\pm)}} \cong [1 \mp \delta(\theta)]. \quad \text{(A11)}$$

The above allows one to show the validity of the following equalities:

$$I_{3.1}(+, -) \stackrel{\text{def}}{=} \int \frac{d\xi}{2\pi}\left[G_{(+)}^2 G_{(+)}^{(\text{rev})}\right]G_{(-)}$$

$$= \frac{i}{[2\epsilon_n s(\epsilon_n)]^2}\begin{cases} [2i|\epsilon_n|s(\epsilon_n) - \gamma(\theta)]^{-1}, & \epsilon_n > 0 \\ [2i|\epsilon_n|s(\epsilon_n) + \gamma(\theta)]^{-1}, & \epsilon_n < 0, \end{cases} \quad \text{(A12)}$$

$$I_{3.1}(-, +) \stackrel{\text{def}}{=} \int \frac{d\xi}{2\pi}\left[G_{(-)}^2 G_{(-)}^{(\text{rev})}\right]G_{(+)}$$

$$= \frac{i}{[2\epsilon_n s(\epsilon_n)]^2}\begin{cases} [2i|\epsilon_n|s(\epsilon_n) + \gamma(\theta)]^{-1}, & \epsilon_n > 0 \\ [2i|\epsilon_n|s(\epsilon_n) - \gamma(\theta)]^{-1}, & \epsilon_n < 0, \end{cases} \quad \text{(A13)}$$

where

$$\gamma(\theta) = 2\alpha(\theta)p_F. \quad \text{(A14)}$$

Hence

$$I_{3.1}(+, -) + I_{3.1}(-, +) = \frac{2}{[2|\epsilon_n|s(\epsilon_n)]Z(\epsilon_n, \theta)}, \quad \text{(A15)}$$

where

$$Z(\epsilon_n, \theta) = [2|\epsilon_n|s(\epsilon_n)]^2 + \gamma^2(\theta). \quad \text{(A16)}$$

Also

$$I_{2.2}(+, -) \stackrel{\text{def}}{=} \int \frac{d\xi}{2\pi}\left[G_{(+)}G_{(+)}^{(\text{rev})}\right]\left[G_{(-)}G_{(-)}^{(\text{rev})}\right]$$

$$= \frac{2}{[2|\epsilon_n|s(\epsilon_n)]Z(\epsilon_n, \theta)}. \quad \text{(A17)}$$

Further, for integrals

$$I_{2.1}(\mu) \stackrel{\text{def}}{=} \int \frac{d\xi}{2\pi}\frac{p(\xi)}{p_F}[G_{(\mu)}]^2 G_{(\mu)}^{(\text{rev})}, \quad \text{(A18)}$$

$$I_{1.2}(\mu) \stackrel{\text{def}}{=} \int \frac{d\xi}{2\pi}\frac{p(\xi)}{p_F}G_{(\mu)}\left[G_{(\mu)}^{(\text{rev})}\right]^2, \quad \text{(A19)}$$

we have

$$I_{2.1}(\mu) = I_{1.2}(\mu) = [1 - 2\delta(\theta)\operatorname{sgn}\mu]\frac{i\operatorname{sgn}\epsilon_n}{[2|\epsilon_n|s(\epsilon_n)]^2}. \quad \text{(A20)}$$

Hence

$$I_{2.1}(+) + I_{2.1}(-) = \frac{2i\operatorname{sgn}\epsilon_n}{[2|\epsilon_n|s(\epsilon_n)]^2}, \quad \text{(A21)}$$

$$I_{2.1}(+) - I_{2.1}(-) = -4\delta(\theta)\frac{i\operatorname{sgn}\epsilon_n}{[2|\epsilon_n|s(\epsilon_n)]^2}. \quad \text{(A22)}$$

It is also valid that

$$I_{2.1}(+, -) \stackrel{\text{def}}{=} \int \frac{d\xi}{2\pi} [G_{(+)}G_{(+)}^{(\text{rev})}]G_{(-)}$$

$$= \frac{i\operatorname{sgn}\epsilon_n}{[2\epsilon_n s(\epsilon_n)]^2 - 2i\epsilon_n s(\epsilon_n)\gamma(\theta)}, \quad \text{(A23)}$$

$$I_{2.1}(-, +) \stackrel{\text{def}}{=} \int \frac{d\xi}{2\pi} [G_{(-)}G_{(-)}^{(\text{rev})}]G_{(+)}$$

$$= \frac{i\operatorname{sgn}\epsilon_n}{[2\epsilon_n s(\epsilon_n)]^2 + 2i\epsilon_n s(\epsilon_n)\gamma(\theta)}. \quad \text{(A24)}$$

From here, it follows that

$$I_{2.1}(+, -) + I_{2.1}(-, +) = \frac{2i\operatorname{sgn}\epsilon_n}{[2|\epsilon_n|s(\epsilon_n)]^2 + \gamma^2(\theta)} \quad \text{(A25)}$$

is an odd function of ϵ_n, whereas

$$I_{2.1}(+, -) - I_{2.1}(-, +) = \frac{-2\gamma(\theta)}{[2|\epsilon_n|s(\epsilon_n)Z(\epsilon_n, \theta)} \quad \text{(A26)}$$

is an even function of ϵ_n. Also with the adopted accuracy

$$I_{2.2}(\mu) \stackrel{\text{def}}{=} \int \frac{d\xi}{2\pi} [G_{(\mu)}G_{(\mu)}^{(\text{rev})}]^2$$

$$= 2\frac{1 - \delta(\theta)\operatorname{sgn}\mu}{[2|\epsilon_n|s(\epsilon_n)]^3}, \quad \text{(A27)}$$

$$J_3 \stackrel{\text{def}}{=} \int \frac{d\xi}{2\pi} \frac{p(\xi)}{p_F} \left\{ \left(\frac{p}{m}\sin\theta + \alpha\right)[G_{(+)}^{(\text{rev})}]^2 G_{(+)} \right.$$

$$\left. - \left(\frac{p}{m}\sin\theta - \alpha\right)[G_{(-)}^{(\text{rev})}]^2 G_{(-)} \right\}$$

$$\cong 2\alpha[1 - 3\sin^2\theta]\frac{i\operatorname{sgn}\epsilon_n}{[2|\epsilon_n|s(\epsilon_n)]^2}, \quad \text{(A28)}$$

and

$$J_4 \stackrel{\text{def}}{=} \int \frac{d\xi}{2\pi} \left(\frac{p}{p_F}\right) \left\{ \left(\frac{p}{m}\sin\theta + \alpha\right)^2 [G_{(+)}^{(\text{rev})}G_{(+)}]^2 \right.$$

$$\left. + \left(\frac{p}{m}\sin\theta - \alpha\right)^2 [G_{(-)}^{(\text{rev})}G_{(-)}]^2 \right\}$$

$$\cong \frac{8}{3}\frac{v_F^2}{[2|\epsilon_n|s(\epsilon_n)]^3}. \quad \text{(A29)}$$

It is also valid that

$$I_n \stackrel{\text{def}}{=} \int \frac{d\xi}{2\pi} \frac{1}{[i\epsilon_n s(\epsilon_n) - \xi]^{2-n}[i\epsilon_n s(\epsilon_n) + \xi]^{2+n}}$$

$$= \frac{2^{1-|n|}}{[(2|\epsilon_n|s(\epsilon_n)]^3}, \quad n = -1, 0, 1. \quad \text{(A30)}$$

$$= (-n_{imp}|U|^2)g_{\beta\kappa}T_{\bar\beta\beta|\alpha\bar\alpha}(\epsilon_n)g_{\zeta\alpha}^t$$

FIG. 23. An equivalent form of the equation for the impurity ladder shown in Fig. 9. Here also spin indices on the upper fermion line should be read from left to right, whereas on the lower line they should be read from right to left.

APPENDIX B: IMPURITY LADDER

In this Appendix, the sum of ladder diagrams is derived and, with its help, an expression for the impurity-dressed gap function is obtained. Diagrams forming the impurity ladder are depicted in Fig. 9. The first term, i.e., the impurity field correlator $(-n_{\text{imp}}|U|^2)\delta_{\bar\beta\bar\alpha}\delta_{\zeta\kappa}$, may be represented in the form

$$(-n_{\text{imp}}|U|^2)g_{\beta\kappa}[\delta_{\bar\beta\bar\alpha}\delta_{\alpha\beta}]g_{\zeta\alpha}^t. \quad \text{(B1)}$$

The second term

$$(-n_{\text{imp}}|U|^2)^2 \int_{\mathbf{p}} G_{\bar\beta\bar\alpha}(i\tilde\epsilon, \mathbf{p})G_{\zeta\kappa}^t(-i\tilde\epsilon, -\mathbf{p}), \quad \text{(B2)}$$

by virtue of Eqs. (15)–(18), also admits an analogous representation,

$$(-n_{\text{imp}}|U|^2)g_{\beta\kappa}t_{\bar\beta\beta|\alpha\bar\alpha}^{(1)}g_{\zeta\alpha}^t, \quad \text{(B3)}$$

with

$$t_{\bar\beta\beta|\alpha\bar\alpha}^{(1)}(\epsilon_n) = (-n_{\text{imp}}|U|^2)\int_{\mathbf{p}} G_{\bar\beta\bar\alpha}G_{\alpha\beta}^{(\text{rev})}. \quad \text{(B4)}$$

Note that here

$$n_{\text{imp}}|U|^2 \int_{\mathbf{p}} = \int_0^\pi \frac{1}{2}\sin\theta d\theta \int \frac{d\hat{p}_\perp}{2\pi} \int \frac{d\xi}{2\pi\tau} \frac{p}{p_F}. \quad \text{(B5)}$$

The forms of Eqs. (B1) and (B3) are tempting us to expect that all terms of the ladder have the same spin structure, that is, the sum of all the diagrams have the form

$$(-n_{\text{imp}}|U|^2)g_{\beta\kappa}T_{\bar\beta\beta|\alpha\bar\alpha}(\epsilon_n)g_{\zeta\alpha}^t, \quad \text{(B6)}$$

as shown in Fig. 23. The matrices g and g^t augmenting the spin-matrix T in Eq. (B6) play an auxiliary role; the reduced impurity ladder, the matrix T, is of importance. According to Fig. 23, the first and second terms of $T_{\bar\beta\beta|\alpha\bar\alpha}$ are $\delta_{\bar\beta\bar\alpha}\delta_{\alpha\beta}$ and $t^{(1)}(\bar\beta\beta|\alpha\bar\alpha)$, consequently. They both, just as the whole T matrix, are objects with four spin indices. Such objects admit two types of representations differing by relative position of spin indices. Consider, for example, the second term of the T matrix. In the first representation,

$$t_{\bar\beta\beta|\alpha\bar\alpha}^{(1)} = \sum_i A_{\bar\beta\bar\alpha}^i B_{\alpha\beta}^i \stackrel{\text{def}}{=} \sum_i A^i \underline{\otimes} B^i, \quad \text{(B7)}$$

while in the second representation

$$t^{(1)}_{\bar{\beta}\beta|\alpha\bar{\alpha}} = \sum_i C^i_{\bar{\beta}\beta} D^i_{\alpha\bar{\alpha}} \stackrel{\text{def}}{=} \sum_i C^i \otimes D^i, \tag{B8}$$

where A^i, B^i, C^i, and D^i are some combinations of Pauli matrices. The transition from one representation to the other can be achieved by means of the Fierz identities [13,19]:

$$1 \underline{\otimes} 1 = \tfrac{1}{2}[1 \otimes 1 + (\mathbf{c} \cdot \boldsymbol{\sigma}) \otimes (\mathbf{c} \cdot \boldsymbol{\sigma})$$
$$+ (\mathbf{c} \times \boldsymbol{\sigma})^n \otimes (\mathbf{c} \times \boldsymbol{\sigma})^n],$$

$$(\mathbf{c} \times \boldsymbol{\sigma})^n \underline{\otimes} (\mathbf{c} \times \boldsymbol{\sigma})^n = 1 \otimes 1 - (\mathbf{c} \cdot \boldsymbol{\sigma}) \otimes (\mathbf{c} \cdot \boldsymbol{\sigma}). \tag{B9}$$

The usefulness of the second representation is that it makes easy both the summation of diagrams forming the impurity ladder and an evaluation of a diagram with the impurity ladder. In its first appearance, $t^{(1)}(\bar{\beta}\beta|\alpha\bar{\alpha})$ has the first type form. Indeed, according to Eq. (B4),

$$t^{(1)}(\bar{\beta}\beta \mid \alpha\bar{\alpha}) = \sum_{\mu,\nu=\pm} R_{(\mu\nu)} Q_{(\mu\nu)}, \tag{B10}$$

where

$$R_{(\mu\nu)} = \int \frac{d\hat{p}_\perp}{2\pi} \Pi^{(\mu)}_{\bar{\beta}\bar{\alpha}}(\mathbf{p}) \Pi^{(\nu)}_{\alpha\beta}(\mathbf{p}),$$

$$Q_{(\mu\nu)} = \frac{1}{2} \int_0^\pi \sin\theta \, Q_{(\mu\nu)}(\theta) d\theta, \tag{B11}$$

with

$$Q_{(\mu\nu)}(\theta) = -\int \frac{d\xi}{2\pi\tau} \frac{p}{p_F} G_{(\mu)} G^{(\text{rev})}_\nu. \tag{B12}$$

From Eqs. (15), it follows that

$$R_{(++)} = R_{(--)} = \tfrac{1}{4}\big[1 \underline{\otimes} 1 + \tfrac{1}{2}(\mathbf{c} \times \boldsymbol{\sigma})^i \underline{\otimes} (\mathbf{c} \times \boldsymbol{\sigma})^i\big],$$

$$R_{(+-)} = R_{(-+)} = \tfrac{1}{4}\big[1 \underline{\otimes} 1 - \tfrac{1}{2}(\mathbf{c} \times \boldsymbol{\sigma})^i \underline{\otimes} (\mathbf{c} \times \boldsymbol{\sigma})^i\big]. \tag{B13}$$

By means of Eq. (B9), one can obtain the second-type form of $R_{(\mu\nu)}$:

$$R_{(++)} = R_{(--)} = \tfrac{1}{4}\big[1 \otimes 1 + \tfrac{1}{2}(\mathbf{c} \times \boldsymbol{\sigma})^i \otimes (\mathbf{c} \times \boldsymbol{\sigma})^i\big],$$

$$R_{(+-)} = R_{(-+)} = \tfrac{1}{4}\big[(\mathbf{c} \cdot \boldsymbol{\sigma}) \otimes (\mathbf{c} \cdot \boldsymbol{\sigma}) + \tfrac{1}{2}(\mathbf{c} \times \boldsymbol{\sigma})^i$$
$$\otimes (\mathbf{c} \times \boldsymbol{\sigma})^i\big]. \tag{B14}$$

Further, by dropping terms of the order of δ^2, we have

$$Q_{(++)}(\theta) = \frac{1 - 2\delta(\theta)}{2\tau|\epsilon_n|s(\epsilon_n)},$$

$$Q_{(--)}(\theta) = \frac{1 + 2\delta(\theta)}{2\tau|\epsilon_n|s(\epsilon_n)}, \tag{B15}$$

so

$$Q_{(++)}(\theta) + Q_{(--)}(\theta) = \frac{2}{2\tau|\epsilon_n|s(\epsilon_n)} \tag{B16}$$

does not depend on θ. With the same accuracy,

$$Q_{(+-)}(\theta) + Q_{(-+)}(\theta) = \frac{4|\epsilon_n|s(\epsilon_n)}{\tau \, Z(\epsilon_n, \theta)}. \tag{B17}$$

Thus, we get

$$t^{(1)}(\epsilon_n) = \tfrac{1}{2}[w(\epsilon_n) \, 1 \otimes 1 + u(\epsilon_n)(\mathbf{c} \cdot \boldsymbol{\sigma}) \otimes (\mathbf{c} \cdot \boldsymbol{\sigma})$$
$$+ v(\epsilon_n)(\mathbf{c} \times \boldsymbol{\sigma})^i \otimes (\mathbf{c} \times \boldsymbol{\sigma})^i], \tag{B18}$$

with

$$w(\epsilon_n) = \frac{1}{2\tau|\epsilon_n|s(\epsilon_n)},$$

$$u(\epsilon_n) = \frac{1}{2} \int_0^\pi \frac{2\tau|\epsilon_n|s(\epsilon_n)\sin\theta \, d\theta}{[2\tau|\epsilon_n|s(\epsilon_n)]^2 + (2\alpha p_F \tau)^2 \sin^2\theta}, \tag{B19}$$

$$v(\epsilon_n) = \frac{1}{2}[w(\epsilon_n) + u(\epsilon_n)].$$

Note that although the θ integral in all equations of this paper where it is present can be expressed as elementary functions, the integral form is more convenient to deal with. It is easy to verify that the third term of the reduced ladder has the form

$$t^{(2)}_{\bar{\beta}\beta|\alpha\bar{\alpha}}(\epsilon_n) = t^{(1)}_{\bar{\beta}\beta|\gamma\bar{\gamma}}(\epsilon_n) t^{(1)}_{\bar{\gamma}\gamma|\alpha\bar{\alpha}}(\epsilon_n). \tag{B20}$$

From Eq. (B18), it follows that

$$t^{(2)}(\epsilon_n) = \tfrac{1}{2}[w^2(\epsilon_n) \, 1 \otimes 1 + u^2(\epsilon_n)(\mathbf{c} \cdot \boldsymbol{\sigma}) \otimes (\mathbf{c} \cdot \boldsymbol{\sigma})$$
$$+ v^2(\epsilon_n)(\mathbf{c} \times \boldsymbol{\sigma})^i \otimes (\mathbf{c} \times \boldsymbol{\sigma})^i]. \tag{B21}$$

Now it is seen that

$$T(\epsilon_n) = t^{(1)}(\epsilon_n) + t^{(2)}(\epsilon_n) + \dots \tag{B22}$$

is the sum of three independent geometrical progressions:

$$T(\epsilon_n) = \frac{1}{2}\left[\frac{1 \otimes 1}{1 - w(\epsilon_n)} + \frac{(\mathbf{c} \cdot \boldsymbol{\sigma}) \otimes (\mathbf{c} \cdot \boldsymbol{\sigma})}{1 - u(\epsilon_n)} \right.$$
$$\left. + \frac{(\mathbf{c} \times \boldsymbol{\sigma})^i \otimes (\mathbf{c} \times \boldsymbol{\sigma})^i}{1 - v(\epsilon_n)} \right]. \tag{B23}$$

It is this form of the impurity ladder which will be used everywhere below. In the dirty limit, i.e., at $T_C\tau \ll 1$ and $\eta = 2\alpha p_F \tau \ll 1$, it follows from Eqs. (B19) that

$$w(\epsilon_n) \cong 1 - 2\tau|\epsilon_n|,$$

$$u(\epsilon_n) \cong 1 - 2\tau|\epsilon_n| - \frac{2}{3}\eta^2. \tag{B24}$$

$$1 - v(\epsilon_n) \cong 2\tau|\epsilon_n| + \frac{1}{3}\eta^2.$$

Now consider the impurity renormalization of the gap function. The second term on the right-hand side of the equation depicted in the upper line in Fig. 10 in view of Eq. (B6) has the form

$$g_{\bar{\beta}\kappa} T_{\beta\bar{\beta}|\bar{\gamma}\gamma} g^t_{\phi\gamma}(-n_{\text{imp}}|U|^2)$$
$$\times \int_\mathbf{p} G^{(0)}_{\gamma\zeta}(i\tilde{\epsilon}, \mathbf{p}) g_{\zeta\xi} \Delta\big[g^t G^{(\text{rev})}(i\tilde{\epsilon}_n, \mathbf{p}) g\big]_{\xi\phi}, \tag{B25}$$

which, subject to Eq. (B23), takes the form

$$g_{\bar{\beta}\kappa} \frac{1}{2} \frac{\delta_{\beta\bar{\beta}}\delta_{\bar{\gamma}\gamma}}{1 - w(\epsilon_n)}(-n_{\text{imp}}|U|^2)$$
$$\times \int_\mathbf{p} G^{(0)}_{\gamma\zeta}(i\tilde{\epsilon}_n, \mathbf{p}) G^{(\text{rev})}_{\zeta\bar{\gamma}}(i\tilde{\epsilon}_n, \mathbf{p})\Delta. \tag{B26}$$

Here, with the adapted accuracy, we have

$$(n_{\text{imp}}|U|^2) \int_{\mathbf{p}} G_{\gamma\zeta}^{(0)}(i\tilde{\epsilon}_n, \mathbf{p}) G_{\zeta\bar{\gamma}}^{(\text{rev})}(i\tilde{\epsilon}_n, \mathbf{p}) \cong \frac{\delta_{\gamma\bar{\gamma}}}{2|\epsilon_n|\tau s(\epsilon_n)}.$$
(B27)

Further, from Eqs. (B19) and (14), it follows that

$$\frac{1}{1 - w(\epsilon_n)} = s(\epsilon_n).$$
(B28)

From Eqs. (B26)–(B28), we see the validity of the equation on the lower line in Fig. 10.

APPENDIX C: DIAGRAMS IN FIG. 8

In this Appendix, we evaluate the part of F_{an} represented by diagrams in Fig. 8. Each of the diagrams can be represented as a product of two factors. The first of these S (it will be called the slow factor) stems from the integration of functions that slowly vary in *coordinate* space: the vector potential $\mathbf{A}(\mathbf{q})$, the magnetic field $\mathbf{B}(\mathbf{q})$, and the gap function $\Delta(\mathbf{q})$. Arguments of these functions in *momentum* space will be called slow variables. The second factor Q (it will be called the quick factor) appears as a result of integration over the momentum $\mathbf{p}$ (or $\mathbf{p}$ and $\mathbf{p}'$) of the fermion lines, taking a trace (in the clockwise direction) over spin variables of all entities entering an electron loop and summing over the fermion frequency ϵ_n. The slow factor S_{an} common to all the diagrams in Fig. 8 is given by

$$S_{\text{an}} = \int_{\mathbf{q}, \mathbf{q}'} B_m(-\mathbf{q}) \Delta\left(\mathbf{q}' + \frac{\mathbf{q}}{2}\right) \Delta^*\left(\mathbf{q}' - \frac{\mathbf{q}}{2}\right) q_j'$$

$$= \int_{\mathbf{r}} B_m(\mathbf{r}) V_j(\mathbf{r}),$$
(C1)

where $\mathbf{V}(\mathbf{r})$ was defined by Eq. (24). Consider the diagram Fig. 8(1v), which does not contain the impurity ladder. It is a symmetric bubble in the sense that it contains an equal number, namely, two, of the direct G and reversed $G^{(\text{rev})}$ Green's functions. Its quick factor, on account of the equality

$$g^t[-\mathbf{v}^t(-\mathbf{p})]g = \mathbf{v}(\mathbf{p}),$$
(C2)

has the form

$$Q_{(1v)} = T \sum_n s^2(\epsilon_n) \int_{\mathbf{p}} \text{Tr}\{\boldsymbol{\sigma}_m G(i\tilde{\epsilon}_n, \mathbf{p})$$

$$\times G^{(\text{rev})}(i\tilde{\epsilon}_n, \mathbf{p}) v_j(\mathbf{p}) G^{(\text{rev})}(i\tilde{\epsilon}_n, \mathbf{p}) G(i\tilde{\epsilon}_n, \mathbf{p})\}, \quad (C3)$$

where

$$\int_{\mathbf{p}} = \int \left(\frac{mp}{\pi}\right) \frac{d\xi}{2\pi} \int \frac{d\hat{p}_\perp}{2\pi} \int_0^\pi \sin\theta \frac{d\theta}{2}.$$
(C4)

The main component of Eq. (C3) is the function

$$I_1(\theta) \overset{\text{def}}{=} \int \left(\frac{mp}{\pi}\right) \frac{d\xi}{2\pi} \int \frac{d\hat{p}_\perp}{2\pi} \{\boldsymbol{\sigma}_m G(i\tilde{\epsilon}, \mathbf{p})$$

$$\times G^{(\text{rev})}(i\tilde{\epsilon}, \mathbf{p}) v_j(\mathbf{p}) G^{(\text{rev})}(i\tilde{\epsilon}, \mathbf{p}) G(i\tilde{\epsilon}, \mathbf{p})\}.$$

$$= \int \frac{d\xi}{\pi} \left(\frac{mp}{\pi}\right) \sum_{\mu\nu} S_{mj}^{(\mu\nu)}(\theta) P_{(\mu\nu)}(\theta),$$
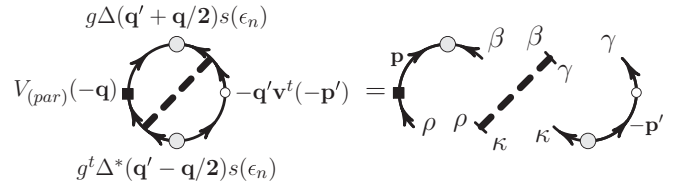(C5)

FIG. 24. The split form of Fig. 8(2v).

where $S_{mj}^{(\mu\nu)}(\theta)$ was defined by Eq. (A5) and

$$P_{(\mu\nu)}(\theta) = \left[G_{(\mu)}^{(0)} G_{(\mu)}^{(\text{rev})}\right]\left[G_{(\nu)}^{(0)} G_{(\nu)}^{(\text{rev})}\right].$$
(C6)

Elements of $S_{mj}^{(\mu\nu)}$ diagonal in indices μ and ν contribute to $I_1(\theta)$

$$\frac{1}{2} e_{mjs} c^s \left(\frac{mp_F}{\pi}\right) (1 - 3\sin^2\theta) \frac{4\alpha}{[2|\epsilon_n|s(\epsilon_n)]^3},$$
(C7)

while the nondiagonal elements contribute

$$\frac{1}{2} e_{mjs} c^s \left(\frac{mp_F}{\pi}\right) \frac{4\alpha}{2|\epsilon_n|s(\epsilon_n)Z(\epsilon_n, \theta)}.$$
(C8)

Since $1 - 3\sin^2\theta = -1 + (2 - 3\sin^2\theta)$ and

$$\int_0^\pi d\theta \sin\theta (2 - 3\sin^2\theta) = 0,$$
(C9)

Eq. (C7), if it is under the sign of the θ integral, can be substituted by

$$\frac{1}{2} e_{mjs} c^s \left(\frac{mp_F}{\pi}\right) \frac{-4\alpha}{[2\epsilon_n s(\epsilon_n)]^3}.$$

As a result,

$$\int_0^\pi I_1(\theta) \frac{\sin\theta}{2} d\theta$$

$$= -4\alpha \, e_{mjs} c^s \left(\frac{mp_F}{\pi}\right) \int_0^\pi d\theta \frac{\sin\theta}{2} \frac{\gamma^2(\theta)}{[2|\epsilon_n|s(\epsilon_n)]^3 Z(\epsilon_n, \theta)}.$$
(C10)

Thus we obtain

$$Q_{(1v)} = e_{jms} c^s Q_{(sy)},$$

$$Q_{(sy)} = T \sum_n s^2(\epsilon_n) 2\alpha \left(\frac{mp_F}{\pi}\right)$$

$$\times \int_0^\pi d\theta \frac{\sin\theta}{2} \frac{\gamma^2(\theta)}{[2|\epsilon_n|s(\epsilon_n)]^3 Z(\epsilon_n, \theta)}.$$
(C11)

Now consider the diagram Fig. 8(2v). It can be represented in a split form as is shown in Fig. 24. Accordingly,

$$Q_{(2v)} = (-n_{\text{imp}}|U|^2) T \sum_{\epsilon_n} s^2(\epsilon_n)$$

$$\times \text{Tr}\{L(\epsilon_n) \circ T(\epsilon_n) \circ R(\epsilon_n)\}.$$
(C12)

Here the left fragment of the diagram,

$$L_{\rho\beta}(\epsilon_n) = \int_{\mathbf{p}} \left\{ G^{(0)}(i\tilde{\epsilon}_n, \mathbf{p})\sigma_m G^{(0)}(i\tilde{\epsilon}_n, \mathbf{p})G^{(\mathrm{rev})}(i\tilde{\epsilon}_n, \mathbf{p}) \right\}_{\rho\beta}$$

$$= \int_{\mathbf{p}} \sum_{\mu\nu} G_{(\nu)} G_{(\mu)} G^{(\mathrm{rev})}_{(\mu)} \left\{ \Pi^{(\nu)}\sigma_m \Pi^{(\mu)} \right\}_{\rho\beta}, \qquad (C13)$$

on account of Eq. (A2), takes the form

$$L_{\rho\beta}(\epsilon_n) = \int d\theta \frac{\sin\theta}{2} \int \frac{d\xi}{2\pi}\left(\frac{mp}{\pi}\right)$$

$$\times \left\{ \left[G^{(\mathrm{rev})}_{(+)} G^2_{(+)} + G^{(\mathrm{rev})}_{(-)} G^2_{(-)} \right]\frac{1}{4}[\sigma_m - c_m(\mathbf{c}\sigma)] \right.$$

$$\left. + G_{(+)} G_{(-)}\left[G^{(\mathrm{rev})}_{(-)} + G^{(\mathrm{rev})}_{(+)} \right]\frac{1}{4}[\sigma_m + c_m(\mathbf{c}\sigma)] \right\}_{\rho\beta}$$

$$(C14)$$

and further can be transformed to

$$L_{\rho\beta}(\epsilon_n) = -\frac{i\,\mathrm{sgn}\,\epsilon_n}{2}\left(\frac{mp_F}{\pi}\right)\int d\theta \frac{\sin\theta}{2}$$

$$\times \left[\frac{\sigma_m - c_m(\mathbf{c}\sigma)}{[2|\epsilon_n|s(\epsilon_n)]^2} + \frac{\sigma_m + c_m(\mathbf{c}\sigma)}{Z(\epsilon_n,\,\theta)} \right]_{\rho\beta}. \quad (C15)$$

Analogously, the right fragment of the diagram,

$$R_{\gamma\kappa}(\epsilon_n)$$

$$= \int_{\mathbf{p}} \left\{ G^{(rev)}(i\tilde{\epsilon}_n, \mathbf{p})v_j(\mathbf{p})G^{(rev)}(i\tilde{\epsilon}_n, \mathbf{p})G(i\tilde{\epsilon}_n, \mathbf{p}) \right\}_{\gamma\kappa}$$

$$= \int_{\mathbf{p}} \sum_{\mu\nu} G^{(rev)}_{(\nu)} G^{(rev)}_{(\mu)} G_{(\mu)} \left\{ \Pi^{(\nu)}v_j(\mathbf{p})\Pi^{(\mu)} \right\}_{\gamma\kappa}, \quad (C16)$$

first, on account of Eq. (A4), takes the form

$$R(\epsilon_n) = \frac{1}{4}(\mathbf{c}\times\boldsymbol{\sigma})^j_{\gamma\kappa}\left(\frac{mp_F}{\pi}\right)\int d\theta \frac{\sin\theta}{2}\int \frac{d\xi}{2\pi}\left(\frac{p}{p_F}\right)$$

$$\times \left\{ \left(\frac{p}{m}\sin\theta + \alpha \right)[G^{(rev)}_{(+)}]^2 G_{(+)} \right.$$

$$- \left(\frac{p}{m}\sin\theta - \alpha \right)[G^{(rev)}_{(-)}]^2 G_{(-)}$$

$$\left. + \alpha\left[G^{(rev)}_{(+)} G^{(rev)}_{(-)} G_{(-)} + G^{(rev)}_{(-)} G^{(rev)}_{(+)} G_{(+)} \right] \right\} \quad (C17)$$

and then, on account of Eq. (A28), takes the form

$$R(\epsilon_n) = -\frac{i}{2}\mathrm{sgn}\,\epsilon_n\left(\frac{mp_F}{\pi}\right)\alpha(\mathbf{c}\times\boldsymbol{\sigma})_j$$

$$\times \int d\theta \frac{\sin\theta}{2}\frac{\gamma^2(\theta)}{[2|\epsilon_n|s(\epsilon_n)]^2 Z(\epsilon_n,\,\theta)}. \quad (C18)$$

In the middle part given by Eq. (B23), one can retain only the term

$$\frac{1}{2}\frac{(\mathbf{c}\times\boldsymbol{\sigma})^t_{\beta\rho}(\mathbf{c}\times\boldsymbol{\sigma})^t_{\kappa\gamma}}{1 - v(\epsilon_n)}. \quad (C19)$$

As a result, the quick factor of Fig. 8(2v) takes the form

$$Q_{(2v)} = e_{jmi}c^i Q_{(l)},$$

$$Q_{(l)} = \frac{\alpha}{2\tau}\left(\frac{mp_F}{\pi}\right)T\sum_{\epsilon_n}\frac{s^2(\epsilon_n)}{1 - v(\epsilon_n)}$$
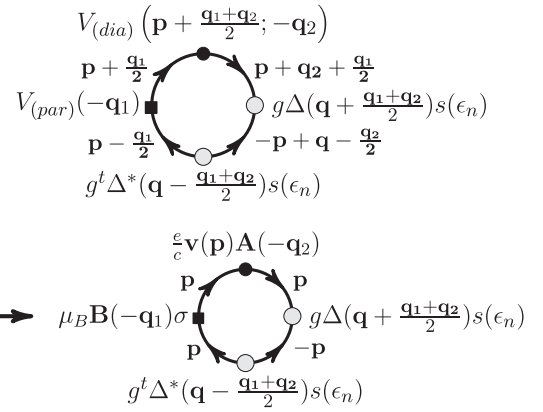

FIG. 25. The detailed form of the left diagram on the first line in Fig. 11.

$$\times \int_0^\pi d\theta \frac{\sin\theta}{2}\int_0^\pi d\theta'\frac{\sin\theta'}{2}$$

$$\times \left[\frac{[2|\epsilon_n|s(\epsilon_n)]^2 + Z(\epsilon_n,\,\theta)}{[2|\epsilon_n|s(\epsilon_n)]^2 Z(\epsilon_n,\,\theta)} \right]$$

$$\times \left[\frac{\gamma^2(\theta)}{[2|\epsilon_n|s(\epsilon_n)]^2 Z(\epsilon_n,\,\theta')} \right]. \quad (C20)$$

Furthermore, one can verify that $Q_{(3v)} = Q_{(2v)}$ and also that the sum of contributions of all the diagrams of the lower line in Fig. 8 is equal to that of the upper line. Thus, the diagrams of Fig. 8 form a linear functional:

$$\mathcal{F}\{\mathbf{B(r)}, \mathbf{V(r)}\} = D\int_{\mathbf{r}} \mathbf{V(r)}\cdot\mathbf{B(r)}\times\mathbf{c},$$

$$D = [2Q_{(sy)} + 4Q_{(l)}]\mu_B. \quad (C21)$$

In the dirty limit, $T_C\tau \ll 1$ and $\eta \ll 1$, Eq. (C11) yields

$$Q_{(sy)} \cong \alpha\frac{4\eta^2}{3}\left(\frac{mp_F}{\pi}\right)T_C\tau\sum_n\frac{1}{(2|\epsilon_n|)^2}, \quad (C22)$$

while Eqs. (C20) yield

$$Q_{(l)} \cong \alpha\frac{4\eta^2}{3}\left(\frac{mp_F}{\pi}\right)T_C\tau\sum_n\frac{1}{(2|\epsilon_n|)^2}\frac{1}{2\tau|\epsilon_n| + \eta^2/3}. \quad (C23)$$

It is seen that the contribution of the diagrams with the impurity ladder dominates.

APPENDIX D: DIAGRAMS IN FIGS. 11 AND 12

Here we evaluate the part of F_{an} which is linear in the vector potential $\mathbf{A(r)}$. The corresponding diagrams are shown in Figs. 11 and 12. Consider Fig. 11(1a). Its complete form is shown in the upper part of Fig. 25. This is an asymmetrical diagram in the sense that it contains three direct Green's functions G and one reversed Green's function $G^{(\mathrm{rev})}$. By dropping the small momenta $\mathbf{q}$, $\mathbf{q}_1$, $\mathbf{q}_2$ from arguments of the fermion lines, we come to the diagram shown in the lower part of Fig. 25. The slow factor of the latter diagram, which is

common to all the diagrams in Figs. 11 and 12, has the form

$$
\mu_B \frac{e}{c} \int_{\mathbf{q},\mathbf{q_1},\mathbf{q_2}} \Delta\left(\mathbf{q} + \frac{\mathbf{q_1} + \mathbf{q_2}}{2}\right) \Delta^*\left(\mathbf{q} - \frac{\mathbf{q_1} + \mathbf{q_2}}{2}\right)
$$

$$
\times B_m(-\mathbf{q_1}) A_j(-\mathbf{q_2}) = \int_{\mathbf{r}} \mu_B B_m(\mathbf{r}) \frac{e}{c} A_j(\mathbf{r}) |\Delta(\mathbf{r})|^2. \quad (D1)
$$

Its quick factor is

$$
Q_{1a} = T \sum_n s^2(\epsilon_n) \int_{\mathbf{p}} \text{Tr}\{\boldsymbol{\sigma}_m G(i\tilde\epsilon_n, \mathbf{p}) v_j(\mathbf{p})
$$

$$
\times G(i\tilde\epsilon_n, \mathbf{p}) G^{(\text{rev})}(i\tilde\epsilon_n, \mathbf{p}) G(i\tilde\epsilon_n, \mathbf{p})\}
$$

$$
= T \sum_n s^2(\epsilon_n) \int d\theta \frac{\sin\theta}{2} \int \frac{d\xi}{2\pi} \left(\frac{mp}{\pi}\right)
$$

$$
\times \sum_{\mu,\nu} S_{mj}^{(\mu\nu)}(\theta)(\mu) G_{(\nu)}^2 G_{(\nu)}^{(\text{rev})}, \quad (D2)
$$

where $S_{mj}^{(\mu\nu)}(\theta)$ is defined by Eq. (A5). Now one can follow the same way as was used in Appendix C to get

$$
Q_{1a} = e_{jms} c^s Q_{(\text{asy})},
$$

$$
Q_{(\text{asy})} = T \sum_n s^2(\epsilon_n) \int d\theta \frac{\sin\theta}{2}
$$

$$
\times \left(\frac{mp_F}{\pi}\right) \frac{\alpha}{[2|\epsilon_n| s(\epsilon_n)]^3} \frac{\eta^2(\theta)}{[2|\epsilon_n| s(\epsilon_n)]^2 + \gamma^2(\theta)}. \quad (D3)
$$

From Eqs. (D3) and (C11), it is seen that

$$
Q_{(\text{asy})} = \tfrac{1}{2} Q_{(\text{sy})}. \quad (D4)
$$

Figure 11(2a) can be evaluated just in the same way as in Fig. 8(2v) with the same result for the quick factor $Q_{2a} = Q_{2v}$. It is also true that $Q_{2a} = Q_{4a} = Q_{5a} = Q_{7a}$, while $Q_{3a} = Q_{1a}$ and $Q_{6a} = 2Q_{1a}$. Thus, all the diagrams in Fig. 11 yield

$$
[2Q_{(\text{sy})} + 4Q_{(l)}] \mu_B \int_{\mathbf{r}} [\mathbf{B}(\mathbf{r}) \times \mathbf{c}] \cdot \frac{e}{c} \mathbf{A}(\mathbf{r}) |\Delta(\mathbf{r})|^2. \quad (D5)
$$

An account of the diagrams in Fig. 12 doubles this result. Now it is seen that the functional defined by the diagrams in Figs. 11 and 12 has the same form as that defined by Eq. (C21), namely,

$$
\mathcal{F}\left\{\mathbf{B}(\mathbf{r}), 2\frac{e}{c}\mathbf{A}(\mathbf{r})\right\}, \quad (D6)
$$

and, being added to C21, forms the gauge-invariant functional

$$
F_{an} = \mathcal{F}\left\{\mathbf{B}(\mathbf{r}), \mathbf{V}(\mathbf{r}) + 2\frac{e}{c}\mathbf{A}(\mathbf{r})\right\}. \quad (D7)
$$

APPENDIX E: CONVENTIONAL TERMS

In an impure system, diagrams in Fig. 13 take the form shown in Fig. 26. Consider Fig. 26(1p). Its slow factor is

$$
S_{1p} = \int_{\mathbf{q}} \Delta^*(\mathbf{q}) \Delta(\mathbf{q}) = \int_{\mathbf{r}} |\Delta(\mathbf{r})|^2, \quad (E1)
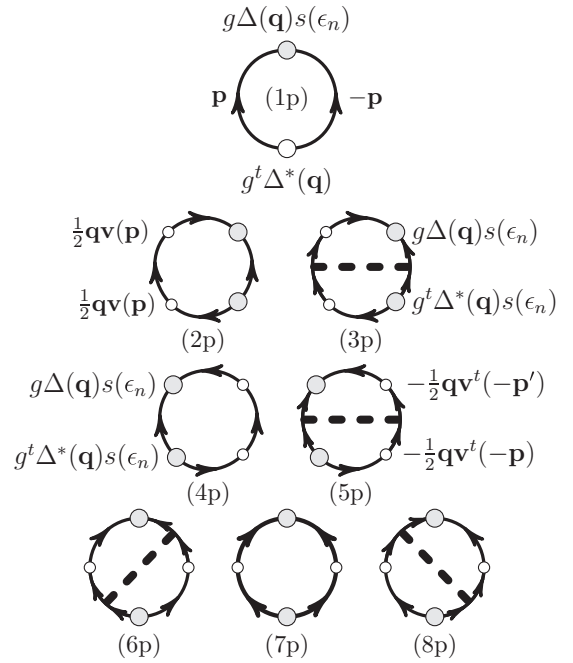$$

FIG. 26. The diagrams in Fig. 13 with the impurity scattering taken into account. They yield the contribution to $\Phi_{2,c}$ of zero order in the magnetic field in an impure superconductor.

while its quick factor is given by

$$
S_{1p} = T \sum_n s(\epsilon_n) \int_{\mathbf{p}} \text{Tr}\{G(i\tilde\epsilon_n, \mathbf{p}) G^{(\text{rev})}(i\tilde\epsilon_n, \mathbf{p})\}
$$

$$
= \int' \left(\frac{mp}{2\pi}\right) \frac{d\xi}{2\pi} \int_0^\pi d\theta \sin\theta \sum_\mu T \sum_n s(\epsilon_n) G_{(\mu)} G_{(\mu)}^{(\text{rev})}, \quad (E2)
$$

where the prime on the ξ-integral restricts the ξ values to the region $|\xi| \leqslant \omega_D$ (ω_D is the Debye frequency, which is assumed to be much greater than T_C). Here the sum $T \sum_n s(\epsilon_n)$ can be transformed into the integral

$$
\int_{-\infty}^\infty \frac{dz}{4\pi i} \tanh \frac{z}{2T} \left[K\left(z, \xi_{(\mu)}, \frac{i}{\tau}\right) - K\left(z, \xi_{(\mu)}, -\frac{i}{\tau}\right)\right], \quad (E3)
$$

with

$$
K\left(z, \xi_{(\mu)}, \pm\frac{i}{\tau}\right) = \frac{1 \pm i/2z\tau}{(z - \xi_{(\mu)} \pm i/2\tau)(z + \xi_{(\mu)} \pm i/2\tau)}. \quad (E4)
$$

To see the independence of Eq. (E2) on τ, note that the difference between the value of the diagram in dirty and clean cases is proportional to the fast converging integral

$$
\int' d\xi \frac{p(\xi)}{p_F} \int_{-\infty}^\infty \frac{dz}{4\pi i} \tanh \frac{z}{2T}
$$

$$
\times \left\{\left[K\left(z, \xi_{(\mu)}, \frac{i}{\tau}\right) - K(z, \xi_{(\mu)}, i0)\right]\right.
$$

$$
\left. - \left[K\left(z, \xi_{(\mu)}, -\frac{i}{\tau}\right) - K(z, \xi_{(\mu)}, -i0)\right]\right\}, \quad (E5)
$$

where one may lift the constrain. After that, the ξ integration makes the integral vanish. In its turn, in the clean case, one may drop the SO coupling by neglecting corrections of the order of δ^2. Thus, just as in the conventional case [7,23], Fig. 26(1p) taken together with the first integral term in Eq. (13) leads to the standard first term in the GL functional given by Eq. (28).

Consider Fig. 26(2p). Its slow factor, which is common to Figs. 26(2p)–26(7p), has the form

$$S_{2p} = \int_{\mathbf{q}} q_i q_j \Delta^*(\mathbf{q})\Delta(\mathbf{q}) = \int_{\mathbf{r}} (\nabla^i \Delta^*(\mathbf{r}))(\nabla^j \Delta(\mathbf{r})). \quad \text{(E6)}$$

Its quick factor is given by

$$Q_{2p} = \frac{1}{4} T \sum_n s^2(\epsilon_n) \int_{\mathbf{p}} \text{Tr}\{G(i\tilde{\epsilon}_n, \mathbf{p})v_i(\mathbf{p})$$
$$\times G(i\tilde{\epsilon}_n, \mathbf{p})v_j(\mathbf{p})G(i\tilde{\epsilon}_n, \mathbf{p})G^{(\text{rev})}(i\tilde{\epsilon}_n, \mathbf{p})\}$$
$$= \frac{1}{4} T \sum_n s^2(\epsilon_n) \int \left(\frac{mp}{2\pi}\right)\frac{d\xi}{2\pi} \int_0^\pi d\theta \sin\theta$$
$$\times \sum_{\mu\nu} P_{ij}^{(\mu\nu)}(\theta)G_{(\mu)}^2 G_{(\nu)}G_{(\mu)}^{(\text{rev})}, \quad \text{(E7)}$$

where $P_{ij}^{(\mu\nu)}(\theta)$ was defined by Eq. (A6). The first term of $P_{ij}^{(\mu\nu)}(\theta)$ [see Eq. (A6)] contributes to Eq. (E7):

$$\frac{1}{4} T \sum_{\epsilon_n} s^2(\epsilon_n) \int \frac{d\xi}{2\pi}\left(\frac{mp}{2\pi}\right)c^i c^j \left(\frac{p}{m}\right)^2$$
$$\times \int_0^\pi d\theta \sin\theta \cos^2\theta \left[G_{(+)}^3 G_{(+)}^{(\text{rev})} + G_{(-)}^3 G_{(-)}^{(\text{rev})}\right]. \quad \text{(E8)}$$

By using results of Appendix A, Eq. (E8) can be transformed to

$$c^i c^j \frac{1}{4} T \sum_{\epsilon_n} s^2(\epsilon_n)\left(\frac{mp_F}{\pi}\right)\frac{2}{3}v_F^2 \frac{1}{[2|\epsilon_n|s(\epsilon_n)]^3}. \quad \text{(E9)}$$

Among contributions of the second term of $P_{ij}^{(\mu\nu)}(\theta)$ to Eq. (E8), only components with $\mu = \nu$ are important; they yield

$$\delta_\perp^{ij} \frac{1}{4} T \sum_{\epsilon_n} s^2(\epsilon_n)\left(\frac{mp_F}{\pi}\right)\frac{2}{3}v_F^2 [2|\epsilon_n|s(\epsilon_n)]^{-3}. \quad \text{(E10)}$$

Thus,

$$Q_{2p} = \delta^{ij} \frac{1}{4} D_{2p},$$
$$D_{2p} = \frac{2v_F^2}{3}\left(\frac{mp_F}{\pi}\right)T \sum_{\epsilon_n} s^2(\epsilon_n)[2|\epsilon_n|s(\epsilon_n)]^{-3}. \quad \text{(E11)}$$

It is easy to see that $Q_{4p} = Q_{2p}$.

Turn to the diagram (7p). Its quick factor has the form

$$Q_{7p} = \frac{1}{4} T \sum_{\epsilon_n} s^2(\epsilon_n) \int_{\mathbf{p}} \text{Tr}\{G(i\tilde{\epsilon}_n, \mathbf{p})v_i(\mathbf{p})$$
$$\times G(i\tilde{\epsilon}_n, \mathbf{p})G^{(\text{rev})}(i\tilde{\epsilon}_n, \mathbf{p})v_j(\mathbf{p})G^{(\text{rev})}(i\tilde{\epsilon}_n, \mathbf{p})\}. \quad \text{(E12)}$$
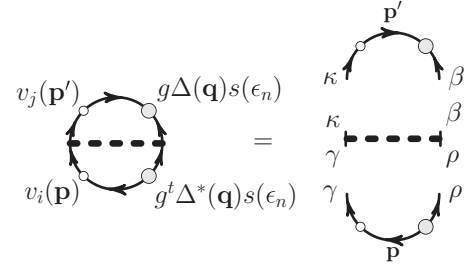

FIG. 27. The split form of Fig. 26(3p).

Just as in the case of Fig. 26(2p), one can show that the first term of $P_{ij}^{(\mu\nu)}(\theta)$ contributes to Eq. (E12),

$$c^i c^j \frac{v_F^2}{3}\left(\frac{mp_F}{\pi}\right)T \sum_{\epsilon_n} s^2(\epsilon_n)[2|\epsilon_n|s(\epsilon_n)]^{-3}, \quad \text{(E13)}$$

while the second term of $P_{ij}^{(\mu\nu)}(\theta)$ gives

$$(\delta_{ij} - c_i c_j)\frac{v_F^2}{3}\left(\frac{mp_F}{\pi}\right)T \sum_{\epsilon_n} s^2(\epsilon_n)[2|\epsilon_n|s(\epsilon_n)]^{-3}. \quad \text{(E14)}$$

Thus, $Q_{7p} = 2Q_{2p}$.

A contribution of a conventional diagram with the impurity ladder contains an additional small factor δ^2 as against the diagram without the ladder. Consider, for example, Fig. 26(3p) shown in a split form in Fig. 27. Its quick factor, according to Fig. 27, is

$$Q_{3p} = (-n_{\text{imp}}|U|^2)T \sum_{\epsilon_n} s^2(\epsilon_n)\text{Tr}\{T_{3p} \circ T(\epsilon_n) \circ B_{3p}\}, \quad \text{(E15)}$$

where the top T_{3p} and bottom B_{3p} parts are

$$T_{3p} = \int_{\mathbf{p}} G^{(\text{rev})}(i\tilde{\epsilon}_n, \mathbf{p})G(i\epsilon_n, \mathbf{p})v_i(\mathbf{p})G(i\tilde{\epsilon}_n, \mathbf{p}) \quad \text{(E16)}$$

and

$$B_{3p} = \int_{\mathbf{p}} G(i\tilde{\epsilon}_n, \mathbf{p})v_j(\mathbf{p})G(i\tilde{\epsilon}_n, \mathbf{p})G^{(\text{rev})}(i\tilde{\epsilon}_n, \mathbf{p}), \quad \text{(E17)}$$

respectively. For the top part, we have

$$T_{3p} = \int \left(\frac{mp}{2\pi}\right)\frac{d\xi}{2\pi} \int_0^\pi d\theta \sin\theta$$
$$\times \sum_{\mu\nu} V_i^{(\mu\nu)}(\theta)G_{(\mu)}^{(\text{rev})}G_{(\mu)}G_{(\nu)}, \quad \text{(E18)}$$

where $V_i^{(\mu\nu)}(\theta)$ was defined by Eq. (A4). The first term in $V_i^{(\mu\nu)}(\theta)$ [see Eq. (A4)] contributes zero to T_{3p} because the integral $\int_0^\pi \sin\theta\cos\theta f(\theta) = 0$ for any function $f(\theta)$. Elements with $\mu = \nu$ of the second term in $V_i^{(\mu\nu)}(\theta)$ contribute to T_{3p}

$$(n_{\text{imp}}|U|^2)\alpha(\mathbf{c}\times\boldsymbol{\sigma})^i \left(\frac{mp_F}{2\pi}\right)\frac{i\,\text{sgn}\epsilon_n}{[2\epsilon_n s(\epsilon_n)]^2}, \quad \text{(E19)}$$

while the elements with $\mu = -\nu$ contribute

$$(n_{\text{imp}}|U|^2)\alpha(\mathbf{c}\times\boldsymbol{\sigma})^i \left(\frac{mp_F}{2\pi}\right)\int_0^\pi d\theta \frac{\sin\theta}{2}\frac{i\,\text{sgn}\epsilon_n}{Z(\epsilon_n, \theta)}. \quad \text{(E20)}$$
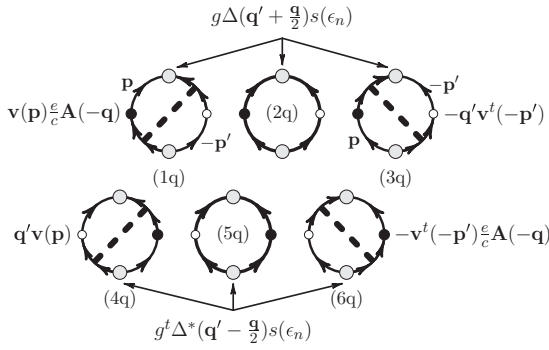
FIG. 28. The diagrams in Fig. 14 with allowance for the impurity scattering. They yield the contribution to $\Phi_{2,c}$ linear in the vector potential in an impure superconductor.

In all,

$$T_{3p} = -i \, \text{sgn} \epsilon_n \frac{\alpha}{2} (\mathbf{c} \times \boldsymbol{\sigma})_i \left(\frac{m p_F}{2\pi} \right)$$
$$\times \int_0^\pi d\theta \, \sin\theta \frac{\gamma^2(\theta)}{[2\epsilon_n s(\epsilon_n)]^2 Z(\epsilon_n, \theta)}. \quad \text{(E21)}$$

By following the same way, one can show that $B_{3p} = T_{3p}$. Since

$$\text{Tr}\{(\mathbf{c} \times \boldsymbol{\sigma})_i \circ T(\epsilon_n) \circ (\mathbf{c} \times \boldsymbol{\sigma})_j\} = \frac{\delta_{ij} - c_i c_j}{1 - v(\epsilon_n)}, \quad \text{(E22)}$$

we get

$$Q_{3p} = \alpha^2 (\delta_{ij} - c_i c_j) \left(\frac{m p_F}{2\pi} \right) \frac{1}{\tau}$$
$$\times \left\{ \int_0^\pi d\theta \frac{\sin\theta}{2} \frac{\gamma^2(\theta)}{[2|\epsilon_n|s(\epsilon_n)]^2 Z(\epsilon_n, \theta)} \right\}^2. \quad \text{(E23)}$$

We see that Q_{3p} is smaller than Q_{2p} by a factor of $(\alpha/v_F)^2$. This estimate also refers to Figs. 26(5p), 26(6p), and 26(8p). Thus the major part of the sum of the quick factors of Figs. 26(2p)–26(8p) is $Q_{2p} + Q_{4p} + Q_{7p} = D_{2p}$. Thus, Figs. 26(2p)–26(8p) contribute to Φ_2

$$D_{2p} \int_{\mathbf{r}} |\nabla \Delta(\mathbf{r})|^2. \quad \text{(E24)}$$

Consider diagrams in Fig. 14, whose contribution to $\Phi_{2,c}$ is linear in the vector potential $\mathbf{A}(\mathbf{r})$. In an impure system, they take the form shown in Fig. 28. The slow factor of each of the diagrams has the form

$$S_q = \int_{\mathbf{q}, \mathbf{q}'} \frac{e}{c} A_i(-\mathbf{q}) q'_j \Delta^* \left(\mathbf{q}' - \frac{1}{2}\mathbf{q} \right) \Delta \left(\mathbf{q}' + \frac{1}{2}\mathbf{q} \right)$$
$$= \frac{e}{c} \int_{\mathbf{r}} A_i(\mathbf{r}) V_j(\mathbf{r}). \quad \text{(E25)}$$

Here also the major contributions to quick factor come from Figs. 28(2q) and 28(5q) without the impurity ladder and $Q_{2q} = Q_{5q} = Q_{7p}$. Thus, for the sum of the diagrams we get

$$D_{2p} \int_{\mathbf{r}} \frac{2e}{c} \mathbf{A}(\mathbf{r}) \left[\Delta^*(\mathbf{r}) \frac{\nabla}{i} \Delta(\mathbf{r}) + \Delta(\mathbf{r}) \frac{\nabla}{-i} \Delta^*(\mathbf{r}) \right]. \quad \text{(E26)}$$

Now turn to term of Φ_{2c}, which is quadratic in $\mathbf{A}(\mathbf{r})$. The corresponding skeleton diagrams are depicted in Fig. 15;
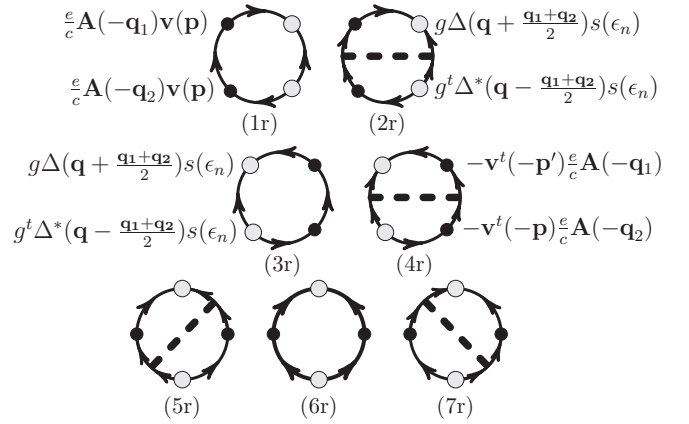

FIG. 29. The diagrams in Fig. 15 with due account of disorder. They yield the contribution to $\Phi_{2,c}$ quadratic in the vector potential in an impure superconductor.

Fig. 29 shows their form on account of impurity scattering. As usual, the boson momenta $\mathbf{q}, \mathbf{q}_1, \mathbf{q}_2$ may be eliminated from arguments of the fermion lines [for the particular case of Fig. 29(1r), this is shown in Fig. 30] in view of $q/p_F \ll 1$. Then the common slow factor of the diagrams becomes

$$S_r = \int_{\mathbf{q}, \mathbf{q}_1, \mathbf{q}_2} \left(\frac{e}{c} \right)^2 A_m(-\mathbf{q}_1) A_j(-\mathbf{q}_2)$$
$$\times \Delta \left(\mathbf{q} + \frac{\mathbf{q}_1 + \mathbf{q}_2}{2} \right) \Delta^* \left(\mathbf{q} - \frac{\mathbf{q}_1 + \mathbf{q}_2}{2} \right)$$
$$= \left(\frac{e}{c} \right)^2 \int_{\mathbf{r}} A_m(\mathbf{r}) A_j(\mathbf{r}) |\Delta(\mathbf{r})|^2. \quad \text{(E27)}$$

Here once again, the quick factors of diagrams with the impurity ladder are negligible in comparison with diagrams without the ladder and $Q_{6r} = 2Q_{1r} = 2Q_{3r}$. Thus, the $\mathbf{A}$-quadratic term in Φ_{2c} is

$$D_{2p} \int_{\mathbf{r}} |\Delta(\mathbf{r})|^2 \left[\frac{2e}{c} \mathbf{A}(\mathbf{r}) \right]^2. \quad \text{(E28)}$$

As a result, Eqs. (24), (26), and (28) add up to

$$D_{2p} \int_{\mathbf{r}} \left| \left(-i\nabla + \frac{2e}{c} \mathbf{A}(\mathbf{r}) \right) \Delta(\mathbf{r}) \right|^2. \quad \text{(E29)}$$
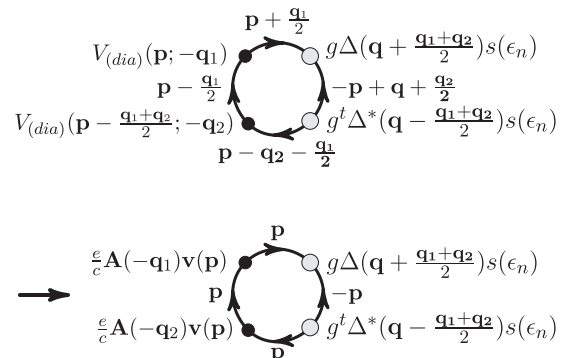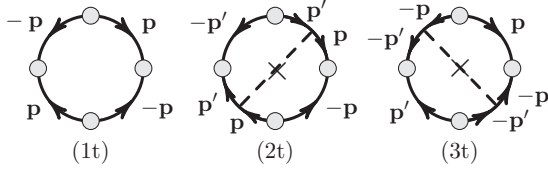

FIG. 30. The detailed representation of Fig. 29(1r).

FIG. 31. The result of the impurity averaging of the diagram in Fig. 16. They are responsible for Φ_4 in an impure superconductor.

Finally, consider the $|\Delta(\mathbf{r})|^4$ term in F_c. For an impure system, diagrams for the term are shown in Fig. 31. The common slow factor of the diagrams is

$$S_4 = \int_{\mathbf{q},\mathbf{q_1},\mathbf{q_2}} \Delta(\mathbf{q})\Delta^*(\mathbf{q_1})\Delta(\mathbf{q_2})\Delta^*(\mathbf{q}+\mathbf{q_2}-\mathbf{q_1})$$

$$= \int_{\mathbf{r}} |\Delta(\mathbf{r})|^4. \tag{E30}$$

The quick factor of Fig. 31(1t) is given by

$$Q_{1t} = T\sum_n s^4(\epsilon_n) \int_{\mathbf{p}} \mathrm{Tr}\big[G(i\tilde{\epsilon}_n,\mathbf{p})G^{(\mathrm{rev})}(i\tilde{\epsilon}_n,\mathbf{p})\big]^2$$

$$= T\sum_n s^4(\epsilon_n) \int \left(\frac{mp}{2\pi}\right)$$

$$\times \frac{d\xi}{2\pi} \int_0^\pi d\theta \sin\theta \sum_\mu \big[G_\mu G_\mu^{(\mathrm{rev})}\big]^2. \tag{E31}$$

Here, just as in any other diagrams for F_c, one can ignore the SO coupling by dropping corrections of the order of δ^2. Then one gets

$$Q_{1t} = \left(\frac{mp_F}{2\pi}\right) T\sum_n \frac{s(\epsilon_n)}{2|\epsilon_n|^3}. \tag{E32}$$

Figures 31(2t) and 31(3t) can also be evaluated by neglecting the SO coupling. Consider Fig. 31(2t). Its split form is shown in Fig. 32. Here the left fragment is

$$L_{2t,\kappa\rho}(\epsilon_n) = s^2(\epsilon_n) \int_{\mathbf{p}} \big\{G^{(\mathrm{rev})}(i\tilde{\epsilon}_n,\mathbf{p})[G(i\tilde{\epsilon}_n,\mathbf{p})]^2\big\}_{\kappa\rho}$$

$$= \delta_{\kappa\rho} N(\epsilon_n), \tag{E33}$$

$$N(\epsilon_n) = s^2(\epsilon_n)\left(\frac{mp_F}{\pi}\right) \frac{i\,\mathrm{sgn}\,\epsilon_n}{[2\epsilon_n s(\epsilon_n)]^2},$$

while the right fragment is $R_{2t,\zeta\gamma}(\epsilon_n) = \delta_{\zeta\gamma} N(\epsilon_n)$. Thus, we get

$$Q_{2t} = (n_{\mathrm{imp}}|U|^2)T\sum_n \mathrm{Tr}\{L_{2t}\circ R_{2t}\}$$

$$= -\left(\frac{mp_F}{2\pi}\right) T\sum_n \frac{1}{4\tau|\epsilon_n|^4}. \tag{E34}$$
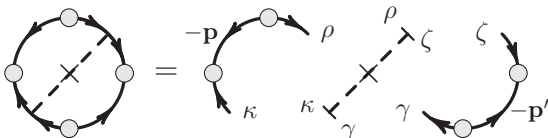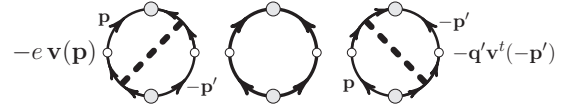

FIG. 32. The split form of Fig. 31(2t).

FIG. 33. The conventional contribution to the current due to the gradient of the phase in a dirty superconductor.

It is evident that $Q_{3t} = Q_{2t}$. From here it follows that

$$Q_{1t} + Q_{2t} + Q_{3t} = \left(\frac{mp_F}{2\pi}\right) T\sum_n \frac{1}{|\epsilon_n|^3}, \tag{E35}$$

which proves Eq. (33) of the main text.

APPENDIX F: ELECTRIC CURRENT

In this Appendix, we outline the derivation of the results Eqs. (35) and (36). Diagrams for the anomalous part of the supercurrent are shown in Fig. 18. Here one can also exclude the slow variables $\mathbf{q}$, $\mathbf{q_1}$, $\mathbf{q_2}$ from arguments of fermion lines. Then the slow factor of each of the diagrams becomes

$$S_{18} = \int_{\mathbf{q_1},\mathbf{q_2}} \Delta^*\Big(\mathbf{q_1}-\frac{\mathbf{q}+\mathbf{q_2}}{2}\Big)\Delta\Big(\mathbf{q_1}+\frac{\mathbf{q}+\mathbf{q_2}}{2}\Big)B_m(-\mathbf{q_2})$$

$$= \int_{\mathbf{r}} |\Delta(\mathbf{r})|^2 B_m(\mathbf{r})e^{-i\mathbf{q}\cdot\mathbf{r}}. \tag{F1}$$

An analysis of quick factors of the diagrams can be performed following the lines of Appendix C. In particular, it can be shown that the contributions of the diagrams Fig. 18(1s) and (3s) are equal and the contribution of the diagram Fig. 18(6s) is twice as large as that of (1s). Also one can show that the contributions of the diagrams Fig. 18(2s), (4s), (5s), and (7s) are equal. As a result, the sum of all quick factors of diagrams in Fig. 18 is the same as the analogous sum of diagrams in Fig. 8, namely, $2Q_{(\mathrm{sy})} + 4Q_{(l)}$, where $Q_{(\mathrm{sy})}$ and $Q_{(l)}$ were defined by Eqs. (C11) and (C20), respectively. Thus

$$\mathbf{J}_{\mathrm{an}}(\mathbf{q}) = -e\mu_B\big[2Q_{(\mathrm{sy})} + 4Q_{(l)}\big]$$

$$\times \int_{\mathbf{r}} e^{-i\mathbf{q}\cdot\mathbf{r}}[\mathbf{B}(\mathbf{r})\times\mathbf{c}]|\Delta(\mathbf{r})|^2. \tag{F2}$$

Conventional part of the current consists of two terms. The first one is defined by the gradient of the gap function; diagrams responsible for the term are shown in Fig. 33. The second part of the conventional current which is due to the presence of the applied magnetic field is depicted in Fig. 34. The slow factor of each diagram in Fig. 33 is

$$S_{33} = \int_{\mathbf{q'}} \mathbf{q'}\Delta^*\Big(\mathbf{q'}-\frac{\mathbf{q}}{2}\Big)\Delta\Big(\mathbf{q'}+\frac{\mathbf{q}}{2}\Big)$$

$$= \int_{\mathbf{r}} e^{-i\mathbf{q}\cdot\mathbf{r}}\mathbf{V}(\mathbf{r}). \tag{F3}$$

The sum of the quick factors of the diagrams in Fig. 33 is the same as the analogous sum of diagrams of the upper line in Fig. 28. Thus, we get

$$\mathbf{J}_c^{(1)}(\mathbf{q}) = -e2D_{2p}\int_{\mathbf{r}} e^{-i\mathbf{q}\cdot\mathbf{r}}\mathbf{V}(\mathbf{r}). \tag{F4}$$
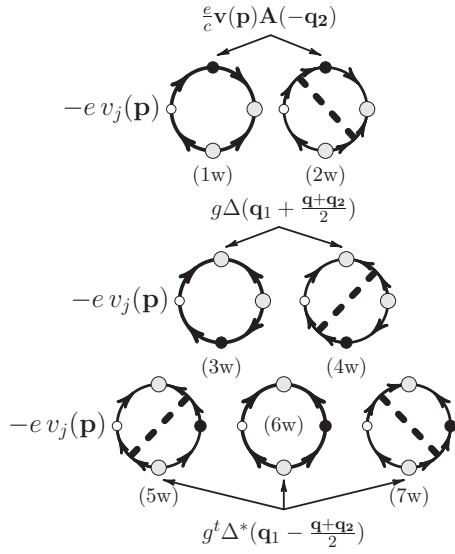
FIG. 34. The diagrams in Fig. 20 with allowance for the impurity scattering. They yield the conventional contribution to the current due to the vector potential in an impure superconductor.

The slow factor of each diagram in Fig. 34 is

$$S_{34} = \int_{\mathbf{q_1},\mathbf{q_2}} \Delta^*\left(\mathbf{q_1} - \frac{\mathbf{q}+\mathbf{q_2}}{2}\right)\Delta\left(\mathbf{q_1} + \frac{\mathbf{q}+\mathbf{q_2}}{2}\right)A_j(-\mathbf{q_2})$$

$$= \int_{\mathbf{r}} e^{-i\mathbf{q}\cdot\mathbf{r}}|\Delta(\mathbf{r})|^2 A_j(\mathbf{r}). \tag{F5}$$

The sum of the quick factors of the diagrams in Fig. 34 is the same as the analogous sum of diagrams in Fig. 29. Thus, we get

$$\mathbf{J}_c^{(2)}(\mathbf{q}) = -2eD_{2p}\int_{\mathbf{r}} e^{-i\mathbf{q}\cdot\mathbf{r}}\frac{2e}{c}\mathbf{A}(\mathbf{r})|\Delta(\mathbf{r})|^2 \tag{F6}$$

so the total conventional current has the form

$$\mathbf{J}_c(\mathbf{r}) = -2e\,D_{2p}\left[\mathbf{V}(\mathbf{r}) + \frac{2e}{c}\mathbf{A}(\mathbf{r})|\Delta(\mathbf{r})|^2\right]. \tag{F7}$$

APPENDIX G: SPIN SUSCEPTIBILITY

The spin susceptibility $\chi_{(s)}$ near T_C has the form

$$\chi_{ij}^{(s)} = \chi_N\left(\delta_{ij} - \frac{\Delta^2}{T_c^2}f_{ij}(T_C\tau, \epsilon_{so}\tau)\right), \tag{G1}$$

where $\chi_N = \mu_B^2(\frac{mp_F}{\pi^2})$ is the spin susceptibility in the normal state. In the dirty limit,

$$f_{ij} = \frac{4}{\pi}T_C\tau\sum_{n\geq 0}\frac{1}{(2n+1)^2}$$

$$\times\left[\frac{c_ic_j}{2\pi T_C\tau(2n+1) + \frac{2}{3}\eta^2} + \frac{\delta_{ij} - c_ic_j}{2\pi T_C\tau(2n+1) + \frac{1}{3}\eta^2}\right]. \tag{G2}$$

Although this result directly follows from a general expression derived earlier [27], in the random phase approximation for any temperatures $T < T_C$, it doesn't seem out of place to derive it here by using the approach adopted in other parts of
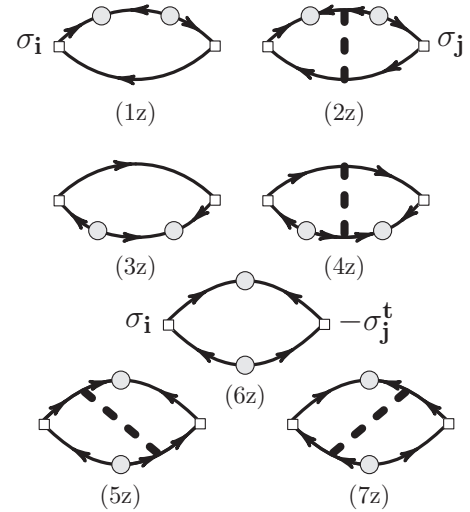
the paper. Diagrams responsible for the deviation of $\chi_{ij}^{(s)} - \chi_N$ are shown in Fig. 35.

The gap functions are considered here as space independent. The quick factor of Fig. 35(1z),

$$Q_{1z} = T\sum_{\epsilon_n}s^2(\epsilon_n)\sum_{\mu\nu}\int_{\mathbf{p}}\text{Tr}\{\sigma_i\Pi^\mu\sigma_j\Pi^\nu\}G_{(\mu)}^2 G_{(\mu)}^{(\text{rev})}G_{(\nu)}$$

$$= T\sum_{\epsilon_n}s^2(\epsilon_n)\int\frac{d\xi}{2\pi}\frac{mp}{\pi}\int_0^\pi\frac{d\theta}{2}\sin\theta$$

$$\times\sum_{\mu\nu}U_{ij}^{(\mu\nu)}G_{(\mu)}^2 G_{(\mu)}^{(\text{rev})}G_{(\nu)}, \tag{G3}$$

can be transformed to the form

$$Q_{1z} = \left(\frac{mp_F}{\pi}\right)T_c\sum_{\epsilon_n}s^2(\epsilon_n)\int_0^\pi\frac{d\theta}{2}\sin\theta$$

$$\times\left\{\frac{2c_ic_j}{[2|\epsilon_n|s(\epsilon_n)]Z(\epsilon_n, \theta)} + (\delta_{ij} - c_ic_j)\right.$$

$$\times\left[\frac{1}{[2|\epsilon_n|s(\epsilon_n)]^3} + \frac{1}{[2|\epsilon_n|s(\epsilon_n)]Z(\epsilon_n, \theta)}\right]\right\}. \tag{G4}$$

Figure 35(2z) can be represented in the split form as shown in Fig. 36. Its quick factor is

$$Q_{2z} = (-n_{\text{imp}}|U|^2)T\sum_{\epsilon_n}s^2(\epsilon_n)$$

$$\times\text{Tr}\{L(\epsilon_n) \circ T(\epsilon_n) \circ R(\epsilon_n)\}. \tag{G5}$$

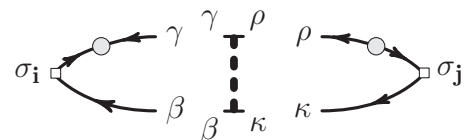FIG. 35. The diagrams for a correction to $\chi_N N$ quadratic in Δ.

FIG. 36. The split form of Fig. 35(2z).

FIG. 37. The diagrams contributing to the spin flow.

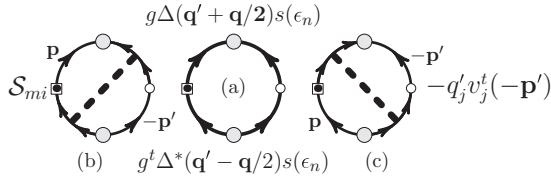FIG. 38. The split form of the diagram (b) in Fig. 37.

Here the left fragment is

$$L_{\beta\gamma}(\epsilon_n) = \left(\frac{mp_F}{\pi}\right) \int_0^\pi \frac{d\theta}{2} \sin\theta \left(\frac{i\,\mathrm{sgn}\epsilon_n}{2}\right)$$
$$\times \left\{\frac{\sigma_i - c_i(\mathbf{c}\boldsymbol{\sigma})}{[2\epsilon_n s(\epsilon_n)]^2} + \frac{\sigma_i + c_i(\mathbf{c}\boldsymbol{\sigma})}{Z(\epsilon_n, \theta)}\right\}_{\beta\gamma}, \quad (G6)$$

the right fragment $R_{\rho\kappa}(\epsilon_n)$ has the same form, the impurity ladder $T(\epsilon_n)$ was defined by Eq. (B23); as a result,

$$Q_{2z} = \left(\frac{mp_F}{\pi}\right) T_C \sum_{\epsilon_n} s^2(\epsilon_n) \left\{\frac{2c_ic_j}{\tau[1 - u(\epsilon_n)]}\right.$$
$$\times \left[\int_0^\pi \frac{d\theta}{2} \sin\theta \frac{1}{Z(\epsilon_n, \theta)}\right]^2 + \frac{\delta_{ij} - c_ic_j}{2\tau[1 - v(\epsilon_n)]}$$
$$\left.\times \left[\int_0^\pi \frac{d\theta}{2} \sin\theta \left(\frac{1}{[[2|\epsilon_n|s(\epsilon_n)]^2} + \frac{1}{Z(\epsilon_n, \theta)}\right)\right]^2\right\}.$$
$$(G7)$$

One can verify that $Q_{(3z)} = Q_{(1z)}$, $Q_{(6z)} = 2Q_{(1z)}$, and $Q_{(4z)} = Q_{(5z)} = Q_{(5z)}$. Thus, the sum of all the diagrams in Fig. 35 gives rise to

$$\chi_{ij}^{(s)} - \chi_N \delta_{ij} = -4[Q_{(1z)} + Q_{(2z)}]\mu_B^2 \Delta^2. \quad (G8)$$

This equation is valid at any relationship between T_C, τ, and ϵ_{SO}; in the dirty limit, it yields Eq. (G2).

APPENDIX H: ABOUT SPIN FLOWS

Diagrams for (the Fourier transform of) the average value of the spin flow operator,

$$\mathcal{S}_{mi} \stackrel{\text{def}}{=} \frac{1}{2}(\sigma_m v_i + v_i \sigma_m)$$
$$= \sigma_m \frac{p_i}{m} + \alpha e_{mis} c^s, \quad (H1)$$

shown in Fig. 37 can be obtained and evaluated following the same way used in the case of the MEE in Sec. VI. Just as in Eq. (F3), by excluding the slow variables $\mathbf{q}$, $\mathbf{q}'$ from the fermion lines, for the slow factor of each of the diagrams we get

$$S_{37} = \int_{\mathbf{r}} e^{-i\mathbf{q}\cdot\mathbf{r}} \mathbf{V}_j(\mathbf{r}). \quad (H2)$$

The quick factor of the diagram (a) has the form

$$Q_{(a)} = T \sum_n s^2(\epsilon_n) \int_{\mathbf{p}} \mathrm{Tr}\{\mathcal{S}_{mi}(\mathbf{p})G(i\tilde{\epsilon}_n, \mathbf{p})$$
$$\times G^{(\mathrm{rev})}(i\tilde{\epsilon}_n, \mathbf{p})v_j(\mathbf{p})G^{(\mathrm{rev})}(i\tilde{\epsilon}_n, \mathbf{p})G(i\tilde{\epsilon}_n, \mathbf{p})\}. \quad (H3)$$

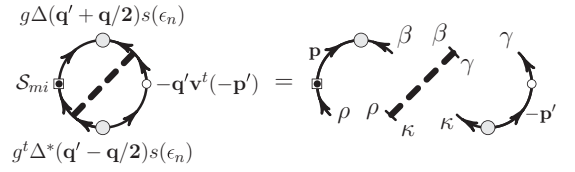The contribution of the second, scalar term of $\mathcal{S}_{mi}$ contains the expression

$$\alpha e_{mis} c^s \delta_{(\mu\nu)} \int \frac{d\hat{p}_\perp}{2\pi} \mathrm{Tr}\{v_j \Pi^{(\mu)}\}$$
$$= \alpha e_{mis} c^s c_j \delta_{(\mu\nu)} \frac{p}{m} \cos\theta \quad (H4)$$

proportional to $\cos\theta$, whereas all Green's functions depend on θ through $\sin\theta$. Since the integral $\int_0^\pi \sin\theta \cos\theta f(\theta) = 0$ for any function $f(\theta)$, the contribution of this term vanishes. The contribution of the first, spin term of $\mathcal{S}_{mi}$ contains the expression

$$H_{mi|j}^{(\mu\nu)} \stackrel{\text{def}}{=} \int \frac{d\hat{p}_\perp}{2\pi} \frac{\hat{p}_\perp^i}{m} Tr\{\sigma_m \Pi^{(\mu)} v_j \Pi^{(\nu)}\}. \quad (H5)$$

With the help of Eq. (A3) and the equality

$$\int \frac{d\hat{p}_\perp}{2\pi} \hat{p}_\perp^i \mathrm{Tr}\{\Pi^{(\mu)}(\mathbf{p})(\boldsymbol{\sigma}\mathbf{B})\Pi^{(\nu)}(\mathbf{p})(\boldsymbol{\sigma}\mathbf{D})\}$$
$$= \frac{i}{2}\begin{pmatrix} 0 & B_i(\mathbf{c}\mathbf{D}) - D_i(\mathbf{c}\mathbf{B}) \\ -B_i(\mathbf{c}\mathbf{D}) + D_i(\mathbf{c}\mathbf{B}) & 0 \end{pmatrix}_{(\mu\nu)}, \quad (H6)$$

which is valid for any 3D vectors $\mathbf{B}$ and $\mathbf{D}$, one can show that

$$H_{mi|j}^{(\mu\nu)} = \delta_{(\mu\nu)}\mathrm{sign}\,\mu \frac{p^2}{2m^2} \cos\theta \sin\theta (e_{mis}c^j + e_{mjs}c^i)$$
$$+ \alpha e_{jsm}c^s c^i \frac{p}{2m} \cos\theta \begin{pmatrix} 1 & 1 \\ 1 & 1 \end{pmatrix}_{(\mu\nu)}$$
$$+ \frac{i}{2}\alpha e_{jsi}c^s c^m \frac{p}{m} \sin\theta \begin{pmatrix} 0 & 1 \\ -1 & 0 \end{pmatrix}_{(\mu\nu)}. \quad (H7)$$

Here contributions of first two terms proportional to $\cos\theta$ vanish by making the θ integration, while the third term turns zero by taking the summation with respect of the helicity states.

Now consider the quick factor of the diagram (b). Figure 38 shows this diagram in the split form. The right fragment of the diagram, which had already been found [see Eq. (C18),

$$R_{\gamma\kappa}(\epsilon_n) = -\frac{i\,\mathrm{sgn}\,\epsilon_n}{2\tau}(\mathbf{c} \times \boldsymbol{\sigma})_{\gamma\kappa}^j \alpha s(\epsilon_n)$$
$$\times \int d\theta' \frac{\sin\theta'}{2} \frac{\gamma^2(\theta')}{[2|\epsilon_n|s(\epsilon_n)]^2 Z(\epsilon_n, \theta')}, \quad (H8)$$

is linear in Pauli matrices. The left fragment is

$$L_{\rho\beta}(\epsilon_n) = \int_{\mathbf{p}} \left[G(i\tilde{\epsilon}_n, \mathbf{p}) \mathcal{S}_{mi}(\mathbf{p}) \right.$$
$$\left. \times G(i\tilde{\epsilon}_n, \mathbf{p}) G^{(\text{rev})}(i\tilde{\epsilon}_n, \mathbf{p}) \right]_{\rho\beta}. \tag{H9}$$

By making use of the equality

$$\int \frac{d\hat{p}_\perp}{2\pi} \Pi^{(\mu)}_{\rho\beta}(\mathbf{p}) = \frac{1}{2}\delta_{\rho\beta}, \tag{H10}$$

the contribution of the second, scalar part of $\mathcal{S}_{mi}$ to $L_{\rho\beta}(\epsilon_n)$ can be put in the form

$$\alpha \, e_{mis} c^s \delta_{\rho\beta} \int \left(\frac{mp}{\pi}\right) \frac{d\xi}{2\pi} \frac{1}{2} \int_0^\pi \sin\theta \frac{d\theta}{2} \sum_\mu G^2_{(\mu)} G^{(\text{rev})}_{(\mu)}, \tag{H11}$$

which is a unit matrix in the spin state and, for this reason, vanishes at the convolution with the impurity ladder and $R_{\gamma\kappa}(\epsilon_n)$. The contribution of first spin part of $\mathcal{S}_{mi}$ to $L_{\rho\beta}(\epsilon_n)$ contains the expression

$$\int \frac{d\hat{p}_\perp}{2\pi} \frac{p_i}{m} \left[\Pi^{(\mu)} \sigma_m \Pi^{(\nu)} \right]_{\rho\beta}$$
$$= c_i \frac{p}{4m} \cos\theta \begin{pmatrix} \sigma_m - c_m(\mathbf{c}\boldsymbol{\sigma}) & \sigma_m + c_m(\mathbf{c}\boldsymbol{\sigma}) \\ \sigma_m + c_m(\mathbf{c}\boldsymbol{\sigma}) & \sigma_m - c_m(\mathbf{c}\boldsymbol{\sigma}) \end{pmatrix}^{(\mu\nu)}_{\rho\beta}$$
$$+ \frac{p}{4m} \sin\theta \left[e_{mis} c^s \delta_{\rho\beta} \begin{pmatrix} 1 & 0 \\ 0 & -1 \end{pmatrix}^{(\mu\nu)} \right.$$
$$\left. - i[c_m\sigma_i - \delta_{mi}(\mathbf{c}\boldsymbol{\sigma})]_{\rho\beta} \begin{pmatrix} 0 & 1 \\ -1 & 0 \end{pmatrix}^{(\mu\nu)} \right]. \tag{H12}$$

This is the sum of tree terms. The first term of Eq. (H12), being proportional to $\cos\theta$, vanishes by making the following θ integration. The second term is a unit matrix in the spin state, and hence vanishes at the convolution with the impurity ladder and $R_{\gamma\kappa}(\epsilon_n)$. The contribution of the third term of Eq. (H12) to $L_{\rho\beta}(\epsilon_n)$ is proportional to

$$G_{(+)} G^{(\text{rev})}_{(+)} G_{(-)} - G_{(-)} G^{(\text{rev})}_{(-)} G_{(+)}$$
$$= \frac{\xi_{(-)} - \xi_{(+)}}{\left[(i\epsilon_n s(\epsilon_n))^2 - \xi^2_{(+)} \right] \left[(i\epsilon_n s(\epsilon_n))^2 - \xi^2_{(-)} \right]}. \tag{H13}$$

This is an even function of ϵ_n, whereas $R_{\gamma\kappa}(\epsilon_n)$ defined by Eq. (H8) is an ϵ_n-odd function. Therefore the third term of Eq. (H12) vanishes at summation with respect to ϵ_n. Thus all the contributions to the diagram (b) vanishes. The diagram (c) vanishes due to the same reasons.

APPENDIX I: 2D SUPERCONDUCTOR

A 2D asymmetric superconductor can be dealt by following the same approach as before. A great simplicity of the 2D case as against the 3D case comes from the fact that the SO splitting of the 2D Fermi surface (the Fermi circle) does not depend on the direction of the electron momentum. Below we present only final results. The coefficients of the GL functional have the following form:

$$A_{(2\text{D})} = \frac{m}{\pi} \left(\frac{T - T_C}{T_C} \right), \tag{I1}$$

$$B_{(2\text{D})} = \frac{m}{2} T_C \sum_{\epsilon_n > 0} \frac{1}{|\epsilon_n|^3}, \tag{I2}$$

$$C_{(2\text{D})} = \frac{m v_F^2}{4} T_C \sum_{\epsilon_n > 0} \frac{1}{s(\epsilon_n)|\epsilon_n|^3}, \tag{I3}$$

$$D_{(2\text{D})} = \left[2Q^{(2\text{D})}_{(\text{sy})} + 4Q^{(2\text{D})}_{(l)} \right] \mu_B, \tag{I4}$$

where

$$Q^{(2\text{D})}_{(\text{sy})} = 2m\alpha T \sum_{\epsilon_n} \frac{s^2(\epsilon_n)(2\alpha p_F)^2}{[2\epsilon_n s(\epsilon_n)]^3 Z_{(2\text{D})}(\epsilon_n)},$$

$$Q^{(2\text{D})}_{(l)} = \frac{m\alpha}{2\tau} T \sum_{\epsilon_n} \frac{s^2(\epsilon_n)(2\alpha p_F)^2}{1 - v_{(2\text{D})}(\epsilon_n)} \frac{[2\epsilon_n s(\epsilon_n)]^2 + Z_{(2\text{D})}(\epsilon_n)}{\{[2\epsilon_n s(\epsilon_n)]^2 Z_{(2\text{D})}(\epsilon_n)\}^2}, \tag{I5}$$

and

$$Z_{(2\text{D})}(\epsilon_n) = [(2\epsilon_n s(\epsilon_n))^2 + (2\alpha p_F)^2],$$
$$v_{(2\text{D})}(\epsilon_n) = \frac{1}{2}(w_{(2\text{D})}(\epsilon_n) + u_{(2\text{D})}(\epsilon_n)), \tag{I6}$$
$$w_{(2\text{D})}(\epsilon_n) = \frac{1}{2\tau|\epsilon_n|s(\epsilon_n)},$$
$$u_{(2\text{D})}(\epsilon_n) = \frac{1}{\tau} \frac{2\tau|\epsilon_n|s(\epsilon_n)}{Z_{(2\text{D})}(\epsilon_n)}.$$

The electric current is given by

$$\mathbf{J}_{2\text{D}}(\mathbf{r}) = -e \, D_{(2\text{D})} [\mathbf{B}(\mathbf{r}) \times \mathbf{c}] |\Delta(\mathbf{r})|^2$$
$$- 2e \, C_{(2\text{D})} \left[\mathbf{V}(\mathbf{r}) + \frac{2e}{c} |\Delta(\mathbf{r})|^2 \right]. \tag{I7}$$

From Eqs. (I4) and (I5), it follows that in the clean limit,

$$D_{(2\text{D})} = \alpha m \mu_B \sum_{\epsilon_n > 0} \frac{(\alpha p_F)^2}{|\epsilon_n|^3 [\epsilon_n^2 + (\alpha p_F)^2]}, \tag{I8}$$

in the dirty limit, when $T_C \tau \ll 1$ and $\epsilon_{\text{SO}} \tau \ll 1$,

$$D_{(2\text{D})} \cong 2\alpha m \mu_B T_c \tau \sum_{\epsilon_n > 0} \frac{1}{\epsilon_n^2} \frac{(2\alpha p_F \tau)^2}{2\tau|\epsilon_n| + 2(\alpha p_F \tau)^2}, \tag{I9}$$

and at $T_C \tau \lesssim 1$ but $\epsilon_{\text{SO}} \tau \gg 1$,

$$D_{(2\text{D})} \cong 2\alpha m \, \mu_B T \sum_{\epsilon_n > 0} \frac{1}{\epsilon_n^2 \left(2\epsilon_n + \frac{1}{2\tau} \right)}. \tag{I10}$$

The latter expression agrees with an analogous result obtained earlier [21] by the quasiclassical method.

It should be noted that in Ref. [21] it is erroneously stated that Ref. [8] concerned 2D systems; the derivation of the GL functional for 3D polar superconductors in the clean limit was really the subject of that work.

[1] *Non-Centrosymmetric Superconductors: Introduction and Overview*, edited by E. Bauer and M. Sigrist (Springer, Heidelberg, 2012).

[2] M. Smidman, M. B. Salamon, H. Q. Yuan, and D. F. Agterberg, Rep. Prog. Phys. **80**, 036501 (2017).

[3] V. M. Edelstein, Phys. Rev. Lett. **75**, 2004 (1995).

[4] S. Yip, Annu. Rev. Condens. Matter Phys. **5**, 15 (2014).

[5] W. Han, Y.-C. Otani, and S. Maekawa, npj Quantum Materials **3**, 27 (2018).

[6] V. L. Ginzburg and L. D. Landau, Zh. Exp. Teor. Fiz. **20**, 1064 (1950).

[7] L. P. Gor'kov, Zh. Eksp. Teor. Fiz. **36**, 1918 (1959) [Sov. Phys. JETP **9**, 1364 (1959)].

[8] V. M. Edelstein, J. Phys.: Condens. Matter **8**, 339 (1996).

[9] L. P. Gor'kov, Zh. Eksp. Teor. Fiz. **37**, 1407 (1959) [Sov. Phys. JETP **10**, 998 (1960)].

[10] W. Xu, Y. Ren, and C. S. Ting, Phys Rev B **53**, 12481 (1996).

[11] T. Shimizu and K. Morigaki, J. Phys. Soc. Jpn. **28**, 1468 (1970).

[12] M. I. Dyakonov and V. I. Perel', Zh. Eksp. Teor. Fiz. **60**, 1954 (1971) [Sov. Phys. JETP **33**, 1053 (1971)].

[13] V. M. Edelstein, J. Phys.: Condens. Matter **5**, 2603 (1993).

[14] E. I. Rashba, Fiz. Tverd. Tela (S.-Peterburg) **2**, 1224 (1960) [Sov. Phys.-Solid State **2**, 1109 (1960)].

[15] R. C. Gasella, Phys. Rev. Lett. **5**, 371 (1960).

[16] F. J. Ohkawa and Y. Uemura, J. Phys. Soc. Jpn. **37**, 1325 (1974).

[17] S. S. Schweber, *An Introduction to Relativistic Quantum Field Theory* (Row, Peterson and Co, Evanston, IL, 1961).

[18] M. Fierz, Zs. f. Phys. **104**, 553 (1937).

[19] P. J. Hirschfeld, P. Wolfle, and D. Einzel, Phys Rev B **37**, 83 (1988).

[20] K. V. Samokhin, Phys Rev B **78**, 224520 (2008).

[21] M. Houzet and J. S. Meyer, Phys. Rev. B **92**, 014509 (2015).

[22] A. A. Abrikosov, L. P. Gor'kov, and I. E. Dzyaloshinskii, *Methods of Quantum Field Theory in Statistical Physics* (Dover, New York, 1963).

[23] A. L. Fetter and J. D. Walecka, *Quantum Theory of Many-Particle Systems* (McGraw-Hill, New York, 1971).

[24] A. A. Abrikosov and L. P. Gor'kov, Zh. Eksp. Teor. Fiz. **35**, 1558 (1958) [Sov. Phys. JETP **8**, 1090 (1959)].

[25] V. M. Edelstein, Phys. Rev. B **72**, 172501 (2005).

[26] *Optical Orientation* edited by F. Meier and B. P. Zacharchenya (North-Holland, Amsterdam, 1984).

[27] V. M. Edelstein, Phys. Rev. B **78**, 094514 (2008).